International Journal of Biological Macromolecules 213 (2022) 352–368

Contents lists available at ScienceDirect

International Journal of Biological Macromolecules

journal homepage: www.elsevier.com/locate/ijbiomac

Thermosensitive chitosan/poly(N-isopropyl acrylamide) nanoparticles embedded in aniline pentamer/silk fibroin/polyacrylamide as an electroactive injectable hydrogel for healing critical-sized calvarial bone defect in aging rat model

Negin Khaneh Zarrin [a], Fatemeh Mottaghitalab [b], Rui L. Reis [c], Subhas C. Kundu [c], Mehdi Farokhi [a,*]

[a] National Cell Bank of Iran, Pasteur Institute of Iran, Tehran, Iran
[b] Nanotechnology Research Centre, Faculty of Pharmacy, Tehran University of Medical Sciences, Tehran, Iran
[c] 3Bs Research Group, I3Bs - Research Institute on Biomaterials, Biodegradable and Biomimetic, Headquarters of the European Institute of Excellence on Tissue Engineering and Regenerative Medicine, University of Minho, AvePark, 4805-017 Barco, Guimaraes, Portugal

ARTICLE INFO

Keywords:
Thermosensitive nanoparticles
Conductivity
Injectable hydrogel
Bone regeneration

ABSTRACT

Thermosensitive nanoparticles with phase transition abilities have been considered as suitable materials in biomedical fields, especially drug delivery systems. Moreover, electroactive injectable hydrogels supporting bone regeneration of the elderly will highly be desired in bone tissue engineering applications. Herein, thermosensitive nanoparticles were fabricated using chitosan/poly(N-isopropyl acrylamide) for simvastatin acid delivery. The nanoparticles were incorporated into electroactive injectable hydrogels based on aniline pentamer/silk fibroin/polyacrylamide containing vitamin C. The nanoparticles had thermosensitive properties as simvastatin acid had higher release rates at 37 than 23 °C without significant burst release. The hydrogels also revealed an appropriate gelation time, stable mechanical and rheological characteristics, high water absorbency, and proper biodegradability. *In vitro* studies indicated that the hydrogel was biocompatible and nontoxic, especially those containing drugs. Implantation of the hydrogels containing both simvastatin acid and vitamin C into the critical calvarial bone defect of the aged rat also demonstrated significant enhancement of bone healing after 4 and 8 weeks post-implantation. We found that the electroactive injectable hydrogels containing thermosensitive nanoparticles exhibited great potential for treating bone defects in the elderly rats

1. Introduction

Bone fracture healing is a complex process, which decreases with age. In the United States, elderly population are increasing, the people aged 65 years and older will comprise 17% of the people by 2030 [1,2]. In aged people, diseases such as osteoporosis and osteoarthritis are prevalent due to physiologic changes in the bone tissues. Many elderlies are susceptible to non-healing bone fractures, resulting in more complicated and systemic consequences [2]. Therefore, it is crucial to design an appropriate strategy based on modern technologies to promote bone regeneration in this population.

The progress in nanotechnology leads to the introduction of many nanostructures for different applications. Designing multifunctional nanomaterials, especially in biomedical applications, is necessary to gain better therapeutic yields. This requirement for adaptation has resulted in the development of stimuli-responsive nanomaterials, also known as smart nanomaterials. These nanomaterials sense various stimuli, including temperature, light, magnetic and electric fields, pressure, stress, and different pH *via* adapting their characteristics, including surface area, shape, size, solubility, permeability, and others [3]. These amazing abilities open a new avenue for using them in numerous applications, including drug delivery, tissue engineering, biosensors, and the treatment of several diseases. Among various stimuli, temperature-responsive (or thermoresponsive) materials have been well-studied in the biomedical fields. Temperature-responsive polymers mostly have hydrophobic functional groups such as propyl, methyl, and

* Corresponding author.
E-mail address: M_farokhi@pasteur.ac.ir (M. Farokhi).

https://doi.org/10.1016/j.ijbiomac.2022.05.176
Received 7 March 2022; Received in revised form 15 May 2022; Accepted 26 May 2022
Available online 28 May 2022

ethyl. The solubility of these materials changes with a small temperature change. Hydrophobic and intra/intermolecular electrostatic interactions break when these polymers face cooling or warming over a critical transition point, resulting in phase transition in the volume [4,5]. Two possible classifications have been introduced based on their temperature-responsive behavior: lower critical solution temperature (LCST) and upper critical solution temperature (UCST). Temperature-responsive polymers with LCST behavior dissolve at temperatures lower than the LCST. Above that, they become hydrophobic because of the formation of polymeric intra- and intermolecular hydrophobic interactions. On the contrary, UCST polymers dissolve above the UCST, and they become insoluble below this temperature due to electrostatic interactions and hydrogen bonding [6,7]. Designing appropriate thermosensitive nanoparticles (NPs) to respond to thermal variability is suitable for delivering various pharmaceutical molecules. One of the reputed smart LCST polymers that have been well-studied is the poly(N-isopropyl acrylamide), or PNIPAM. The current study modified chitosan (CS) NPs by using PNIPAM polymer to fabricate thermosensitive CS/PNIPAM NPs. CS is a biocompatible and biodegradable natural polymer that has been applied as drug nanocarriers for treating various cancers, gastrointestinal diseases, pulmonary, and brain diseases [8]. Jung et al. synthesized and characterized thermosensitive NPs comprising PNIPAM in the core and CS in the shell. The NPs exhibited thermosensitive manners such as LCST and size shrinkage affected by the PNIPAM core and prompted some degrees of particle aggregation around LCST [9]. We also used CS/PNIPAM NPs for delivering simvastatin to treat bone defects. The simvastatin belongs to the statin groups. It is established to have some osteoconductive properties due to enhancing the expression of the bone morphogenetic protein 2 (BMP-2) gene that promotes bone regeneration *in vivo* [10,11]. However, simvastatin absorption is not well. It is necessary to be modified into a metabolically active simvastatin acid (SVA) through the hydrolysis of the ester bond [12]. Herein, CS/PNIPAM NPs containing SVA are known as CS/PNIPAM NPs ^{SVA}. After fabrication of CS/PNIPAM NPs, the NPs were embedded in an injectable hydrogel comprised of silk fibroin (SF)/polyacrylamide (PAAm). SF hydrogels are considered effective candidates for numerous applications owing to their unique biocompatibility and biodegradability [13]. Several methods have been used for fabricating SF hydrogel, for example, ultrasonication, shear action, self-assembly, electric field effect, temperature and pH changes, and others [14]. In the current study, the combination of SF and PAAm was used to prepare an injectable hydrogel as a bone-tissue scaffold. PAAm based hydrogels have been extensively investigated due to their biocompatibility, excellent swelling properties, biological inertness, and thermal stability [15]. Recently, the use of electroactive hydrogels to regenerate and stimulate the repair of electrically active tissues such as bone, skin, muscle, and nerve has received much attention. [16]. Various conductive materials such as graphene and graphene oxide, single- or multi-walled- carbon nanotubes, and poly (3,4-ethylene dioxythiophene) (PEDOT) have been introduced to improve the electrical conductivity of the scaffolds. Nonetheless, non-biodegradability, poor solubility, and induction of chronic inflammation are reported using these materials [17,18]. Conversely, it is possible to use electroactive materials based on oligo conductive and biodegradable parts such as aniline pentamer (AP) due to its high stability, cost-effectiveness, and biodegradability. AP has ability to shift between resistive and conductive statuses by doping/dedoping [19,20]. In our previous work, we fabricated an electroactive injectable hydrogel by inserting AP in pluronic-chitosan polymers. The data confirmed that the fabricated injectable hydrogel was proper for treating ischemic brain defects [21]. Herein, we prepared an injectable hydrogel based on AP-SF/PAAM containing vitamin C (VitC). AP-SF/PAAM hydrogel containing VitC is known as AP-SF/PAAM ^{VitC}. It is confirmed that VitC has a positive role in trabecular bone formation by induction in the expression of bone-specific matrix genes such as alkaline phosphatase (ALP), osteocalcin, osteopontin, osteonectin, and RUNX2 in osteoblasts [22]. Considering the preceding, the aim of the current study was fabricating thermosensitive CS/PNIPAM NPs ^{SVA} incorporating in an electroactive injectable hydrogel based on AP-SF/PAAM ^{VitC} with the ability to promote bone regeneration in the aging rat model. The structure's full name is called CS/PNIPAM NPs ^{SVA}&AP-SF/PAAM ^{VitC} hydrogel.

2. Materials and methods

2.1. Materials

Most of the materials including sodium carbonate, lithium bromide (LiBr), dialysis tubing (12,000 Da cut-off), culture media, fetal bovine serum (FBS), ketamine/xylazine, chitosan (CS), low molecular weight (50,000–190,000 Da), Tripolyphosphate (TPP), N-Isopropylacrylamide (NIPAM) (97%), N,N′- Methylenebis(acrylamide) (Bis), ammonium persulfate (APS), N,N′-Methylenebisacrylamide (NNMBA), *N*, *N*-Dimethyle formamide (DMF), *N*,*N*′-Diphenyl-1,4-phenylenediamine, succinic anhydride, 1-(3-dimethylaminopropyl)-3-ethylcarbodiimide hydrochloride (EDC), n-hydroxysuccinimide (NHS) were purchased from Sigma-Aldrich.

2.2. Preparation of CS/PNIPAM NPs

Firstly, the PNIPAM solution was prepared as follows: NIPAM monomers (30 mg) were dissolved in 250 mL deionized water (DI water), then NNMBA (0.6 mg) as a crosslinking agent and 250 mL APS (24 mg/mL) as an initiator were added to the solution. In order to prepare CS/PNIPAM NPs, 500 μL PNIPAM solution was blended with 500 μL TPP (1% w/v). Afterwards, PNIPAM/TPP solution were slowly added to 3 mL CS solution (1% w/v) dissolved in 1% (v/v) acetic acid at pH 3.5 on magnetic stirrers at 40 °C. Finally, the NPs were collected using centrifugation at 12000 × rpm for 10 min (Sigma high-speed centrifuge, USA). The NPs were finally lyophilized by a freeze dryer (Christ alpha, UK) for further use. Furthermore, CS NPs were also prepared using the routine ionic gelation method [23] as a control group.

2.2.1. Characterization of CS/PNIPAM NPs

Dynamic light scattering (DLS; 3000, HS, Malvern, UK) was used to analyse the size, charge, and polydispersity index (PDI) of the NPs. Uniform dispersion of the NPs was achieved by sonication of lyophilized CS/PNIPAM NPs at 70% amplitude for 10 min in filtered DI water. Further, the field emission scanning electron microscopy (FESEM; TESCAN MIRA3 LMU, Czech Republic) at an accelerating voltage of 15 kV was applied to evaluate the morphology of NPs. About 20 μL of the sonicated NPs suspension was placed on clean laboratory microscope glass slides and then coated with gold under vacuum. It should be noted that all the quantitative experiments were repeated at least three times.

2.3. Preparation of SVA loaded on CS/PNIPAM NPs (CS/PNIPAM NPs ^{SVA})

Firstly, simvastatin was converted to SVA using the following procedure [12]. Compared with unmodified simvastatin, SVA has carboxylic groups that can be activated with EDC/NHS for interaction with amine groups of CS. For this, 42 mg simvastatin was dissolved in 1 mL ethanol (96%), and then 1.5 mL of NaOH (0.1 M) was added to the solution. The resulting solution was stirred for two h at 50 °C. The pH of the mixture was adjusted to 7.4 by using hydrochloric acid (1 M). The total volume of the resulting solution was increased to 10 mL by using DI water. To activate the carboxylic groups of SVA, 1.19 and 5.53 mg of EDC and NHS were added to SVA solution, respectively. The solution was stirred for one h at dark. Finally, the pH of the mixture was adjusted to about 6. To load SVA on CS/PNIPAM NPs, the NPs were dispersed in SVA solution and then sonicated at 50% amplitude for 1 min. Eventually, the sample was stirred for 36 h to complete the interaction. CS/PNIPAM NPs ^{SVA} were recovered by centrifugation at 12000 × rpm for

10 min for further use.

2.4. Loading efficiency and release profile of SVA from CS/PNIPAM NPs

For loading assessment, the supernatant of unbounded SVA was taken and measured by spectrophotometer (Epoch-2 microplate spectrophotometer, United States) at 238 nm using the following formulations:

$$\text{Encapsulation efficiency}(\%) = \frac{\text{Total amount of drug} - \text{unbounded drug}}{\text{The total amount of drug}} \times 100$$

$$\text{Loading capacity}(\%) = \frac{\text{The total amount of drug} - \text{unbounded drug}}{\text{Wight of Nanoparticles}} \times 100$$

To determine the release of SVA from thermosensitive CS/PNIPAM NPs, about 5 mg of NPs were dispersed in phosphate-buffered saline (PBS) and poured into dialysis tubing and then dialyzed against 2 mL PBS in a shaker incubator (shaking at 100 rpm) over 30 days. Further, about 5 mg of NPs were also incorporated in hydrogel to determine the effect of hydrogel on the release rate of the drug. To determine the effect impact of the thermosensitive properties of CS/PNIPAM NPs on the release of SVA, the release of the drug was evaluated at room and body temperatures, 23 and 37 °C, respectively. At the given time, 2 mL of PBS was withdrawn and replaced with identical amounts of fresh PBS. The supernatant was evaluated at 238 nm by using the spectrophotometer. Moreover, Fourier transform infrared spectrophotometry (FTIR; Shimadzu 8400 s; Japan) in transmittance mode was used to analyse the interaction of SVA and CS/PNIPAM NPs in the spectral regions of 400–4000 cm^{-1}.

2.5. Synthesis of aniline pentamer (AP)

According to the previous references [24–26], succinic anhydride (0.05 M) in DMF was added to *N*, *N*′-Diphenyl-1,4-phenylenediamine (0.05 M) dissolved in DMF. The resultant solution was stirred for 48 h in the dark at 37 °C. Subsequently, phenylene diamine (0.025 M) dissolved in DMF was added to the mixture. Then, APS dissolved in hydrochloric acid (1 M) was added to the resultant solution. The mixture was left for 60 min at 37 °C on the stirrer and AP was collected by centrifugation at 3000 × rpm for 10 min. AP powders were characterized by using FTIR analysis.

2.6. Fabrication of electroactive injectable AP-SF/PAAm

Firstly, *Bombyx mori* SF fibers were degummed by boiling them in 0.02 M Na2CO3 for 30 min to remove the glue-like sericin. After washing the degummed SF fibers, they were dissolved in LiBr (9.3 M) at 60 °C for 4 h. Then the yellowish solution was dialyzed against DI water by dialysis tubes (12,000 Da cut-off) for 72 h at 4 °C to remove the residual LiBr salt. The solution was also centrifuged at 5000 rpm for 10 min to remove the impurities. The concentrated SF solution was used for hydrogel preparation as follows. The electroactive injectable hydrogel was prepared by gentle blending of AAm (100 mg), NNMBA (0.5 mg) as cross-linker, APS (50 mg) as thermal initiator, and AP (0.5 mg) as an electro-conductive agent in 500 μL DI water. Simultaneously, SF (20% w/v) was added to the resulting solution. Then the solution was left on the stirrer at 50 °C to a sol-gel transition. A similar procedure was applied to prepare CS/PNIPAM NPs ^{SVA} injectable hydrogel, except that the NPs (5 mg) were added to the PAAm solution. Moreover, the injectable hydrogel without AP and NPs was considered as a control group.

2.7. Characterization of AP-SF/PAAm electroactive injectable hydrogel

2.7.1. Injectability and inversion evaluation

The injectability of the hydrogels was carried out by pouring them into 1 mL syringe and subjecting them to manual shear forces. The extrusion from the 20-gauge needle was examined visually. The inversion test was also implemented to assess the effect of gravity on the hydrogel's flow/stability. In this context, equal volumes of the hydrogels were poured into the glass beakers. The beakers were tilted and then inverted and left undisturbed.

2.7.2. Assessment of hydrogel conductivity

The four-probe method was used to measure the conductivity of the hydrogel. The electrodes were inserted in hydrogels with plate shapes and the conductivity was determined using the following equation:

$$\sigma = 1d/RS$$

Where σ, d, R, and S are conductivity, thickness, resistance, and area of the sample, respectively. Three groups, including SF/PAAm, AP-SF/PAAm, and CS/PNIPAM NPs ^{SVA}&AP-SF/PAAM ^{VitC} hydrogels, were considered for all characterization tests.

2.7.3. Rheology

The gelation temperature, gelation time, and the viscoelasticity of electroactive injectable hydrogels were conducted using a rheological study by a rotational rheometer (Rheometer MCR 302). The temperature sweep evaluation was conducted at various temperatures between 25 and 110 °C. Gelation time was measured at different time points (0–1200 s). Moreover, the frequency sweep test was applied at 1% strain (linear viscoelastic range) at a 1–10 Hz frequency at room temperature.

2.7.4. Mechanical properties

The mechanical properties of electroactive injectable hydrogels were conducted by a mechanical tester (H10KS, Hounsfield, England). The dimensions of the hydrogels were 5.8 mm (diameter) × 11 mm (height). At first, the samples were soaked in DI water and kept at 37 °C. Compression and cyclic compression of the hydrogels were carried out at a crosshead speed of 0.5 $mm.min^{-1}$ under compression mode.

2.7.5. Swelling and degradation ratio

For swelling, the freeze-dried electroactive injectable hydrogels were soaked in PBS for 24 h. The swelling ratio of hydrogels was calculated using the following equation until reaching the plateau.

$$\text{Swelling ratio}(\%) = \frac{W1 - W0}{W0} \times 100$$

Where W_0 displays the initial weight (dry weight) of the hydrogel (mg) and W_1 shows the final weight of the hydrogel after hydration.

For *in vitro* degradation test, the hydrogels were immersed in PBS (pH 7.4) at 37 °C. After various time intervals (every five days), the percentage of weight loss of hydrogels was measured using the equation.

$$\text{Degradation ratio}(\%) = \frac{W0 - W1}{W0} \times 100$$

Where W_0 displays the initial weight (dry weight) of the hydrogel (mg) and W_1 indicates the weight loss of hydrogel at various time points.

The surface morphology of hydrogels was also characterized using FESEM.

2.7.6. Biocompatibility and cell behaviors assessment

Briefly, the extraction solution of the hydrogels was obtained at different time points (1, 5, and 10 days) according to ISO 10993-5 and used for MTT, alkaline phosphatase assay (ALP), and Alizarin red staining analysis studies. For all tests, rabbit osteoblast cells were used that were isolated and characterized, previously [27]. For the MTT

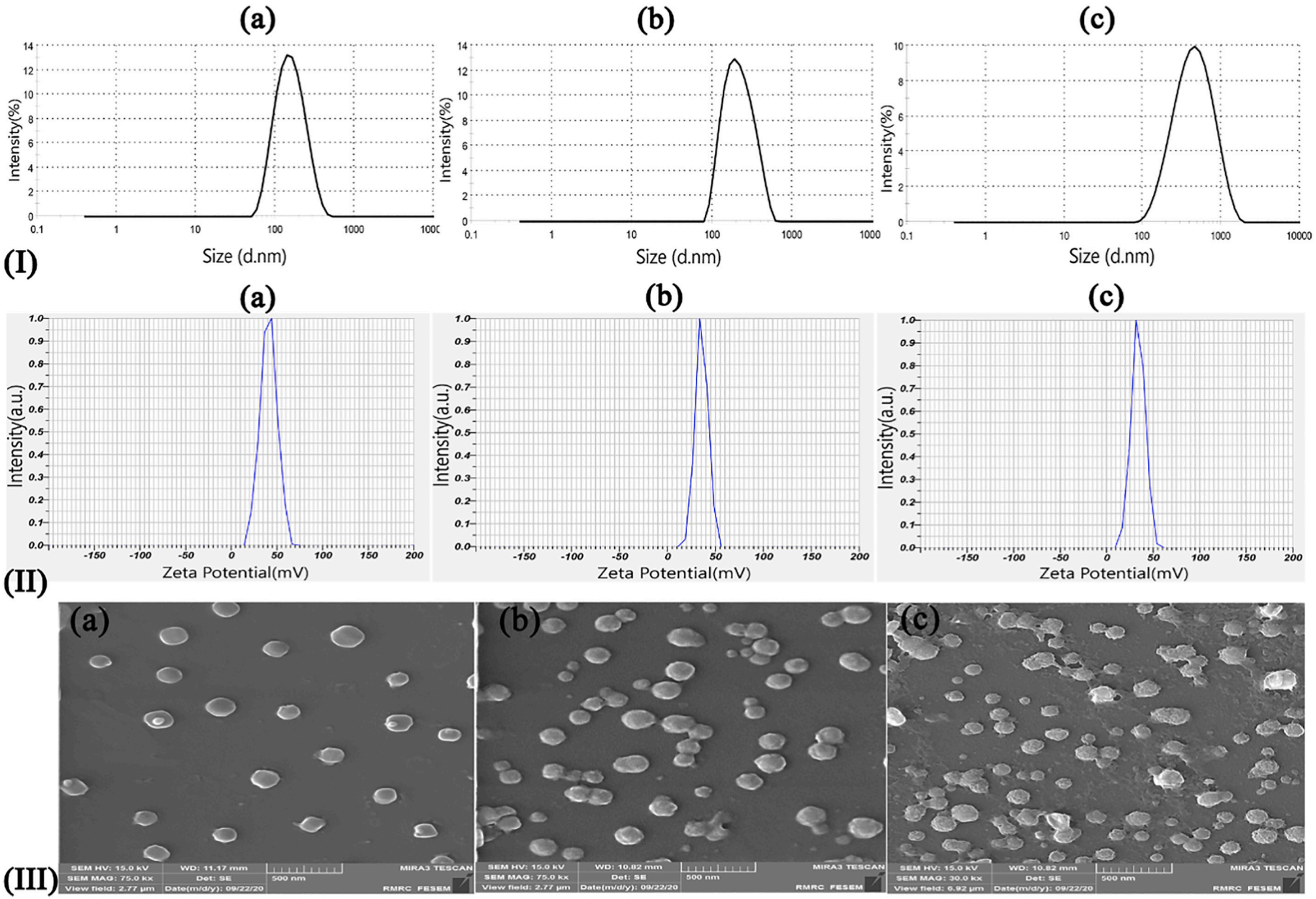

Fig. 1. (I) Size distribution and zeta potential of NPs. The size distribution of: a) CS NPs, b) CS/PNIPAM NPs, and c) CS/PNIPAM NPs loaded SVA. The PDI value of about 0.2 was obtained for all NPs. (II) Zeta potential of: d) CS NPs, e) CS/PNIPAM NPs, and f) CS/PNIPAM NPs loaded SVA. (III) FESEM of: a) CS NPs, b) CS/PNIPAM NPs, and c) CS/PNIPAM NPs loaded SVA. All NPs had nearly spherical morphology, and the size of NPs was increased after drug loading. The data were average values (±SD) of the thrice-repeated measurements. Magnification: 80.0 KX. Scale bar: 500 nm.

assay, about 10×10^4 cells/well in 96-well plates were seeded overnight, and then the culture media was exchanged with the extraction solutions. After 24 h incubation, the extraction solutions were withdrawn and 100 μL of MTT solution (0.5 mg/mL in PBS at pH 7.4) was added to each well for 4 h. Subsequently, the precipitated formazan was dissolved using isopropanol for 30 min. Then the absorbance of each well was read using the spectrophotometer at 570 nm. For all cell analysis studies, the study groups are as follows: tissue culture plate (TCP) as a negative control group, SF/PAAm, AP-SF/PAAm, and CS/PNIPAM NPs ^{SVA}&AP-SF/PAAM ^{VitC} hydrogels.

2.7.7. Lactate dehydrogenase (LDH) assay

LDH is a cytosolic soluble enzyme that is applicable for cell cytotoxicity assessment. About 10×10^5 rabbit osteoblast cells were cultured in the extraction solutions in an incubator for 24 h. The supernatants were used for the analysis of LDH according to the commercial kit. The absorbance was read at 490 nm. The study groups were similar to the MTT assay.

2.7.8. Apoptosis assay

Flow cytometry using Annexin V-FITC/propidium iodide (PI) staining was applied to detect apoptotic cells after incubation in extraction solution obtained from day 10. Based on the manufacturer's protocol, 2×10^5 rabbit osteoblast cells were seeded on 6-well plates overnight. The next day, 1 mL of extraction solution was added and the cells were left for 24 h. Afterwards, the cells were detached and washed twice with PBS and then stained with Annexin V-FITC (5 μL) and PI (5 μL) in dark conditions for 15 min at 23 °C and evaluated by flow cytometry (Beckman coulter FC500).

2.7.9. Alkaline phosphatase activity

For this, about 10×10^4 rabbit osteoblast cells were seeded on 24-well plates overnight and then the culture medium was exchanged with the extraction solutions obtained from 1, 5, and 10 days. The cells were cultured in extraction solutions for 3 days and the ALP activity was assessed using ALP's kit based on the manufacturer's protocol. Finally, the absorbance was read at 405 nm.

2.7.10. Alizarin-Red staining

Cell seeding was similar to the ALP assay. After removing the extraction solutions, the cells were washed twice with NaCl solution and then fixed with 2% paraformaldehyde solution. The Alizarin-Red stain (pH 4.1–4.3) was added for 1 h. Afterwards, the cells were washed with DI water and observed under an optical microscope. For semi-quantitative assessment of calcium deposition, the cells were firstly fixed using methanol and stained with Alizarin-Red stain for 10 min and then washed with PBS. Subsequently, 400 mL of sulfuric acid (10%) was added to each well and left for 30 min. After removing the cellular layers, they were transferred to microtubes and heated at 85 °C for 10 min in a bain-marie bath. Microtubes were centrifuged at 5000 × rpm for 15 min at 4 °C. About 80 μL of the extracts were poured into a 96-well plate and neutralized by 30 μL ammonium hydroxide solution (10%). The absorbance was read at 405 nm.

2.7.11. Cell attachment and morphology study on hydrogels

After hydrogel sterilization, about 10×10^4 rabbit osteoblast cells were seeded on the hydrogels and incubated for 24 h in an incubator. Then, the hydrogels were fixed by glutaraldehyde (2.5%) for 1 h. Serial dilution of ethanol solution (10, 30, 50, 70, 80, 85, 90, 95, and 100%) was used to dehydrate cells. The attached cells on hydrogels were observed under FESEM after gold sputtering.

2.8. In vivo animal studies

Adult 12 months old male Wistar rats were obtained from the Pasteur Institute of Iran. The animals were habituated for at least six days in the animal facility before the surgical process. The animal studies were accomplished based on the Review Board and Ethics Committee of the National Institute for Medical Research Development (IR.NIMAD.REC.1398.048). Briefly, the aged rats were anesthetized using Ketamine (60 mg/kg) and Xylazine (6 mg/kg). After shaving, a longitudinal incision was made in the skull. Then, the skin and periosteum were reflected to expose the calvarial bone. A critical-sized calvarial defect with a 10 mm diameter was made by dental drill micromotor and implanted with the sterile hydrogels. Then, the skin and periosteum were sutured and sterilized using a betadine solution. For sedation of pain after surgery, the animals received painkillers, daily. All groups contain five rats. The study groups are as follows: group 1: bone sockets without hydrogel as the negative control group, group 2: SF/PAAm, group 3: AP-SF/PAAm, and group 4: CS/PNIPAM NPs ^{SVA}&AP-SF/PAAM ^{VitC} hydrogels.

2.8.1. Analysis of bone regeneration using micro-computed tomography (micro-CT)

After implantation for 4 and 8 weeks, the harvested specimens were fixed in a formaldehyde (10%) solution. Micro-CT (LOTUS *in vivo*, Behin Negareh Co., Tehran, Iran) was conducted to analyse bone regeneration in the calvarial defect. The X-ray tube voltage and its current were set to 70 kV and 110 μA, respectively, to achieve the best image quality. The frame exposure time was set to 2 s by 1.4 magnification. Slice thicknesses of reconstructed images were selected to 30 μm. Moreover, LOTUS NDT-3D was applied to render reconstructed images and by addition of the Bone Analysis Plugin (BAP) inside the software, we reported Bone Volume Fraction (BV%).

2.8.2. Histological staining

Four and eight weeks after surgery, the bones were fixed in formalin solution (10%), decalcified in EDTA (10%) for two weeks and then embedded in paraffin. The tissue blocks with 5 μm thicknesses were stained with hematoxylin and eosin (H&E) and Masson's trichrome to evaluate bone repair.

2.9. Statistical analysis

Statistical analyses were conducted using one-way variance (ANOVA) analysis with SPSS 16.0 (SPSS, USA). *P* values of less than 0.05 were regarded as statistically significant.

3. Results and discussion

3.1. Synthesis and characterization of CS/PNIPAM NPs

Thermosensitive biocompatible NPs with the ability to release the drugs upon sensing the body tempreture, is an exciting area in cancer treatment and tissue engineering fields. Recently, numerous researchers have used bulk [28,29] or blended CS polymer [30,31] to fabricate thermosensitive hydrogels to deliver various biomolecules. However, few studies have focused on the perpetration of thermosensitive CS NPs. For example, a thermoresponsive nanoconstruct based on CS-g-poly (N-isopropylacrylamide) *co*-polymeric NPs as a cancer career was fabricated for curcumin delivery [32]. Other thermosensitive CS-g-poly(N-vinyl caprolactam) NPs have also been prepared as a 5-fluorouracil carrier for cancer drug delivery applications [33]. Herein, CS/PNIPAM NPs were successfully synthesized and characterized for delivery of SVA. Compared with CS NPs, the CS/PNIPAM NPs had mono-peak particle size distribution with PDI of about 0.2 based on DLS analysis. PDI values of 0.2 and below are accepted for polymeric-based NPs [34]. The average hydrodynamic diameters of CS NPs, CS/PNIPAM NPs, and CS/PNIPAM NPs ^{SVA} were about 200 ± 3.04, 350 ± 3.08, and 375 ± 4.01, respectively (Fig. 1 (I) a-c). The data revealed that the size of CS NPs was increased after adding PNIPAM. The charge of CS NPs, CS/PNIPAM NPs, and CS/PNIPAM NPs ^{SVA} were about +41 ± 0.34, +35 ± 0.23, and +34 ± 0.31 mV, respectively. Blending PNIPAM with CS had no significant

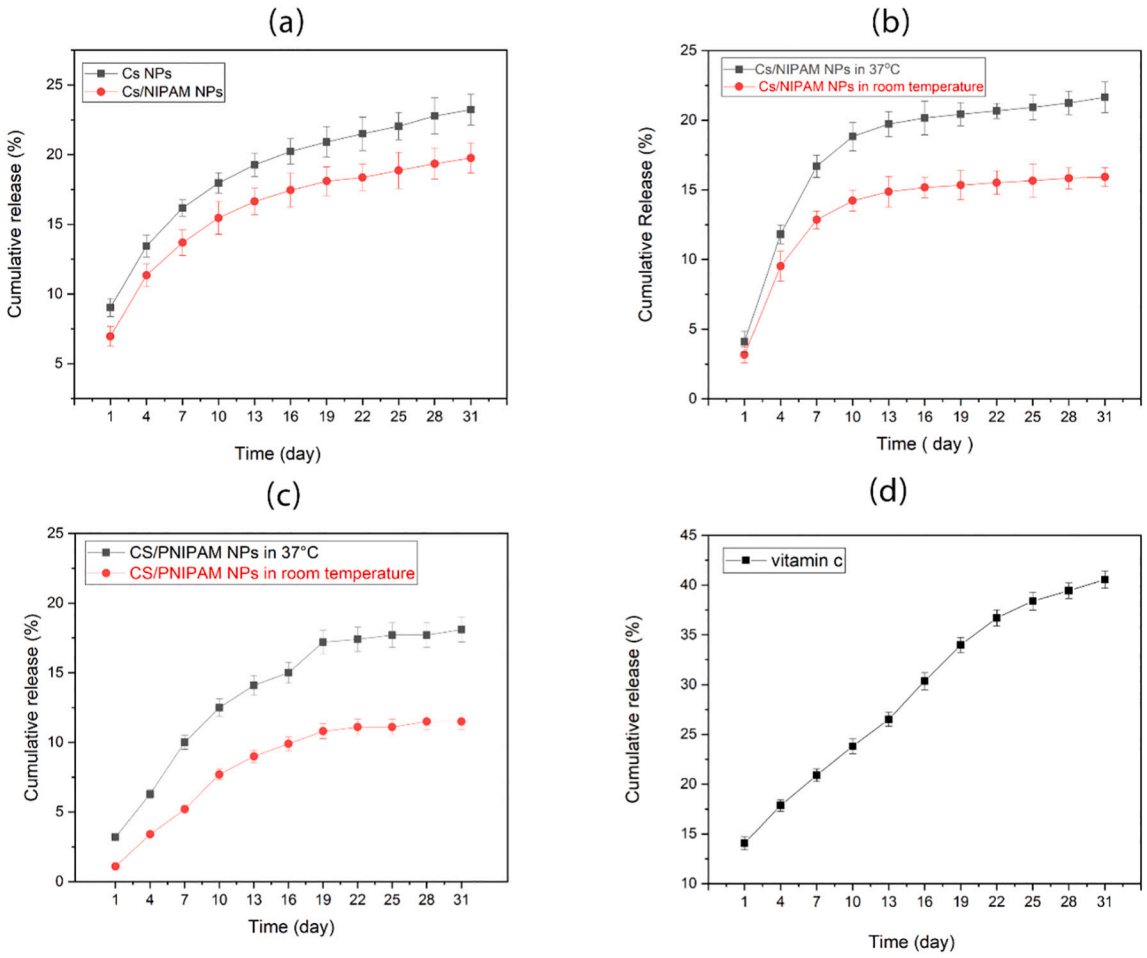

Fig. 2. Release kinetics of the drug from the NPs in PBS solution after 31 days. a) Comparison of the release profile of SVA from CS NPs and CS/PNIPAM NPs at room temperature. b) Comparison of the release profile of SVA from CS/PNIPAM NPs at room and 37 °C temperatures, confirming temperature sensitivity of CS/PNIPAM NPs. C) The release profile of SVA from CS/PNIPAM NPs embedded in hydrogel at room and 37 °C temperatures d) The cumulative release profile of VitC from electroactive injectable AP-SF/PAAm hydrogels after 31 days of incubations. The data were average values (±SD) of thrice-repeated measurements.

change in the zeta potential of CSNPs (Fig. 1 (II) a-c). This result was expected because the amine groups are responsible for the positive charge of CS. Structurally, PNIPAM is neutral, but depending on the method of fabrication, the persistence of some reactants can induce slightly (negative) charge. FESEM analysis was carried to further clarify the size and morphology of NPs (Fig. 1 (III) a-c). FESEM showed that CS NPs were nearly spherical in shape with an average diameter of 178 ± 2.03 nm. The diameters of CS/PNIPAM NPs were about 210 ± 8 nm, whereas it was 230 ± 9 nm for NPs containing drug. No noticeable aggregation occurred for any NPs groups. The increase in diameter of the loaded NPs rather than other groups may be attributed to the successful drug loading on NPs. According to data, the size of NPs obtained from DLS was larger than those observed by FESEM. There are several reasons for this observation. By using DLS technique, it is possible to measure the hydrodynamic radii of the particles. It means that this technique not only measure the diameter of the particle itself but also measure the solvent and ionic layers associated with it in the solution. Further, DLS is a dynamic measurement that is highly sensitive to the aggregation or dispersion of NPs in solution; however, SEM analysis carries out on the dried particles [35].

3.2. Drug delivery assessment

The encapsulation efficiencies of SVA were about 77 and 79%, whereas the loading capacities were about 1.46 and 7.14% for CS NPs and CS/PNIPAM, respectively. The high entrapment of the drug within the NPs may be attributed to the positive charge of CS due to the existence of amine groups in its structure that induced electrostatic binding with the negatively charged SVA [36]. A similar study showed that high loading of simvastatin (more than 90%) was achieved by using CS NPs due to the ionic interaction of the drug with CS [37]. Release kinetics of the drug from the NPs was studied by soaking the NPs in PBS. At predetermined intervals, a given amount of release medium was withdrawn and the amount of SVA was detected using the spectrophotometer. At first, the SVA had a constant release rate without significant burst release from both NPs at room temperature, confirming the successful interactions between the drug and the nanocarriers. The release kinetic showed a biphasic release profile. An initial fast release was observed by the peripherally loaded SVA located in the surface of NPs (<10%) for both CS NPs and CS/PNIPAM NPs after 24 h post-incubation. Afterwards, the SVA was released from the NPs steady-state (Fig. 2a). The release of SVA from CS NPs and CS/PNIPAM NPs was about 19 and 23% over 31 days at room temperature. Subsequently, we investigated the effect of the thermosensitive behavior of CS/PNIPAM NPs on the release kinetics of the drug by evaluating the release profile of SVA at body temperature. The data showed that temperature could affect the drug release. The amount of the released drug from the thermosensitive nanocarriers at 37 °C was more (21%) than those immersed at 23 °C (15%) after 31 days (Fig. 2b). It was also shown that the release of SVA from thermosensitive nanocarriers embedded in the hydrogel was about 18.1 and 11.5% at 37 °C and room temperature, respectively (Fig. 2c). Although embedding thermosensitive NPs in hydrogel decreased SVA's

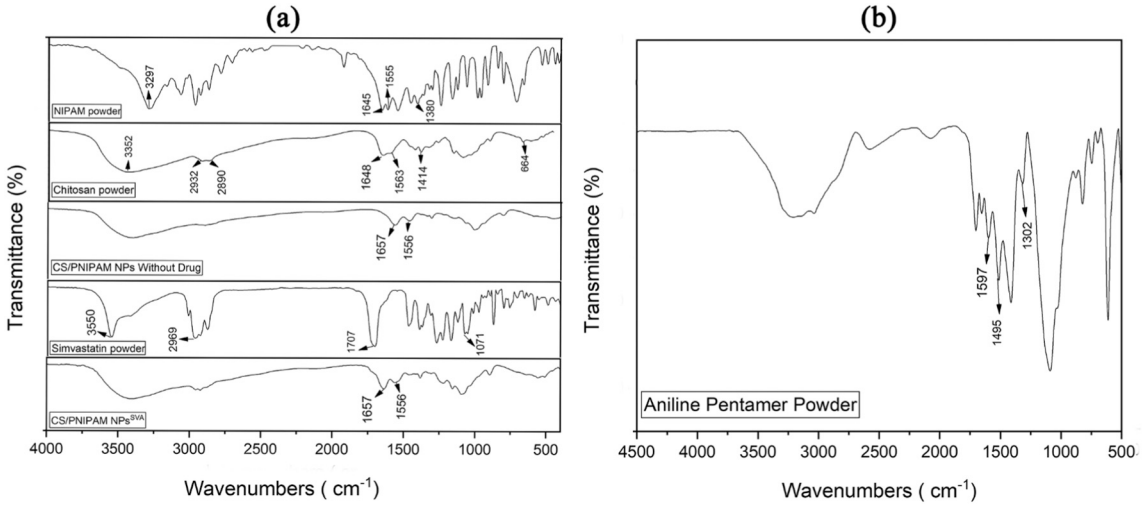

Fig. 3. a) FTIR analysis of NIPAM, CS, CS/PNIPAM NPs, simvastatin, CS/PNIPAM NPs containing SVA (CS/PNIPAM NPs SAV) powders. b) FTIR analysis of aniline pentamer powder.

release rate, it was not significant compared with the release rate of the drug without hydrogel. The slow release rate of SVA from hydrogel containing thermosensitive NPs may be related to the barrier effect of hydrogel that restricts the release of the drug. In a study, only 5% of the drug was released from thermosensitive CS-g-poly (N-isopropyl acrylamide) *co*-polymeric NPs under LCST, but more drugs were released above LCST. The LCST was the primary mechanism for the drug release, at which the high polymer-polymer interaction may be higher than the polymer-drug interaction. In this condition, the loaded drug can release from the polymeric carriers due to expelling water and weakening the hydrogen and electrostatic bonds [32]. Another thermosensitive hydrogel composed of NIPAAm and *N*, *N*′-dimethyl aminopropyl methacrylamide was applied to deliver insulin. This study also showed that the temperature cycling operations could significantly influence the release rate of insulin [38].

As previously mentioned, AP-SF/PAAm hydrogel was loaded with VitC to improve its biological activity. The cumulative release profile of VitC from the hydrogel showed that about 15% of the drug was released after 24 h, possibly due to the high hydrophilicity of VitC. Moreover, the release profile was controlled, and about 40% of the drug was released from the hydrogel after 31 days, indicating suitable delivery of the vitamin *via* the prepared carrier (Fig. 2d). Generally, VitC has a low molecular weight with high water solubility. Consequently, it cannot make strong interactions with polymeric networks, resulting in fast diffusion in an aqueous environment [39]. Recently, it was reported that the release rate of VitC from 3D printed hydrogel based on poly(ethylene glycol) dimethacrylate (PEGDMA) within the first 15 min was about 15%. The release profile was gradually increased and reached equilibrium at six h, which was the total experiment duration [40]. Furthermore, it was shown that the microstructure, such as larger pores and high porosity of composite scaffolds of carboxymethyl CS-SF, could affect the release rate of VitC by increasing the water penetration rate into the scaffolds, which facilitates the release of the water-soluble drug [41]. However, in the current study, the 3D fabricated hydrogels could control the release of VitC for a longer time due to their compact structure that acted as a barrier to the fast release of VitC.

3.3. Characterizing the chemical structure of CS/PNIPAM NPs

FTIR spectra of CS showed the peaks at 3352, 2932, and 2890 cm^{-1} related to OH, –CH2, and –CH3 aliphatic groups, respectively (Fig. 3a). The characteristic absorption bands at 1563 and 1414 cm^{-1} were attributed to NH-group bending vibration and vibrations of the –OH group of the primary alcoholic group, respectively. The peaks in the range of 3400 to 3500 cm^{-1} belonged to the CS amino group that can be masked by the broad absorption peak from the –OH group. The peak at 1648 cm^{-1} may be related to C═O groups [42]. FTIR spectra of NIPAM represented a typical absorption band at 3297 cm^{-1}corresponding to N—H stretching. The vibration bands at 1645 and 1555 cm^{-1} were related to the amide group [O=C–NH]. Further, the band at 1380 cm^{-1} was attributed to the C—H vibrations of the isopropyl group [–CH $(CH_3)_2$] (Fig. 3a) [43].

The bands at 1657 and 1556 cm^{-1} were also observed in the spectra of CS/PNIPAM NPs composite. The peak at 1657 cm^{-1} may be related to the shift of the 1648 cm^{-1} band of CS. Moreover, the peak at 1556 cm^{-1} has corresponded to the amide groups of NIPAM polymer. The results confirmed the presence of CS and PNIPAM within the NPs [44]. Pure simvastatin showed characteristic peaks at 3550, 2969, and 1707 cm^{-1} assigned to the O—H stretch, C—H stretch (alkane), and C═O stretch, respectively. FTIR studies were also conducted to find the possible interactions between the SVA and NPs. The data showed that the CS/PNIPAM NPs SAV group spectra had similar peaks to CS/PNIPAM NPs without drug. In other words, no new peaks were observed after adding SAV to the NPs (Fig. 3a). This finding indicated that the characteristic bands of SAV were probably masked by the peaks of CS and PNIPAM.

Furthermore, AP powders were also characterized by using FTIR analysis (Fig. 3b). The absorption of AP exhibited bands at 1597 and 1495 cm^{-1} corresponding to the absorption of a benzene ring and the quinoid ring. The 1305 cm^{-1} peak was assigned to C—N stretching in the proximity of quinoid rings [45].

3.4. Characterization of injectable electroactive AP-SF/PAAm hydrogels: injectability and conductivity

Most of the bone defects have irregular shapes, and 3D injectable hydrogels with good molding ability have been considered excellent scaffolding material due to their soft structure similar to extracellular matrix (ECM), tunable physical and chemical structures, and the capability of filling any irregularly shaped bone defects [46]. Especially, injectable conductive hydrogels have become a promising candidate for bone tissue engineering. Injectable hydrogels can be injected from a syringe through a fine needle, so the injectability of the hydrogel can be adjusted by simple extrusion of the hydrogel from the needle. In the current study, the flow-ability of the solutions was excellent, and the composite hydrogels were formed after mixing and heating. Macroscopically, the phase transition was observed by changing the transparency appearance of the hydrogel solution into a turbid appearance (Fig. 4 (I) a and b). Moreover, the hydrogel was constantly injected

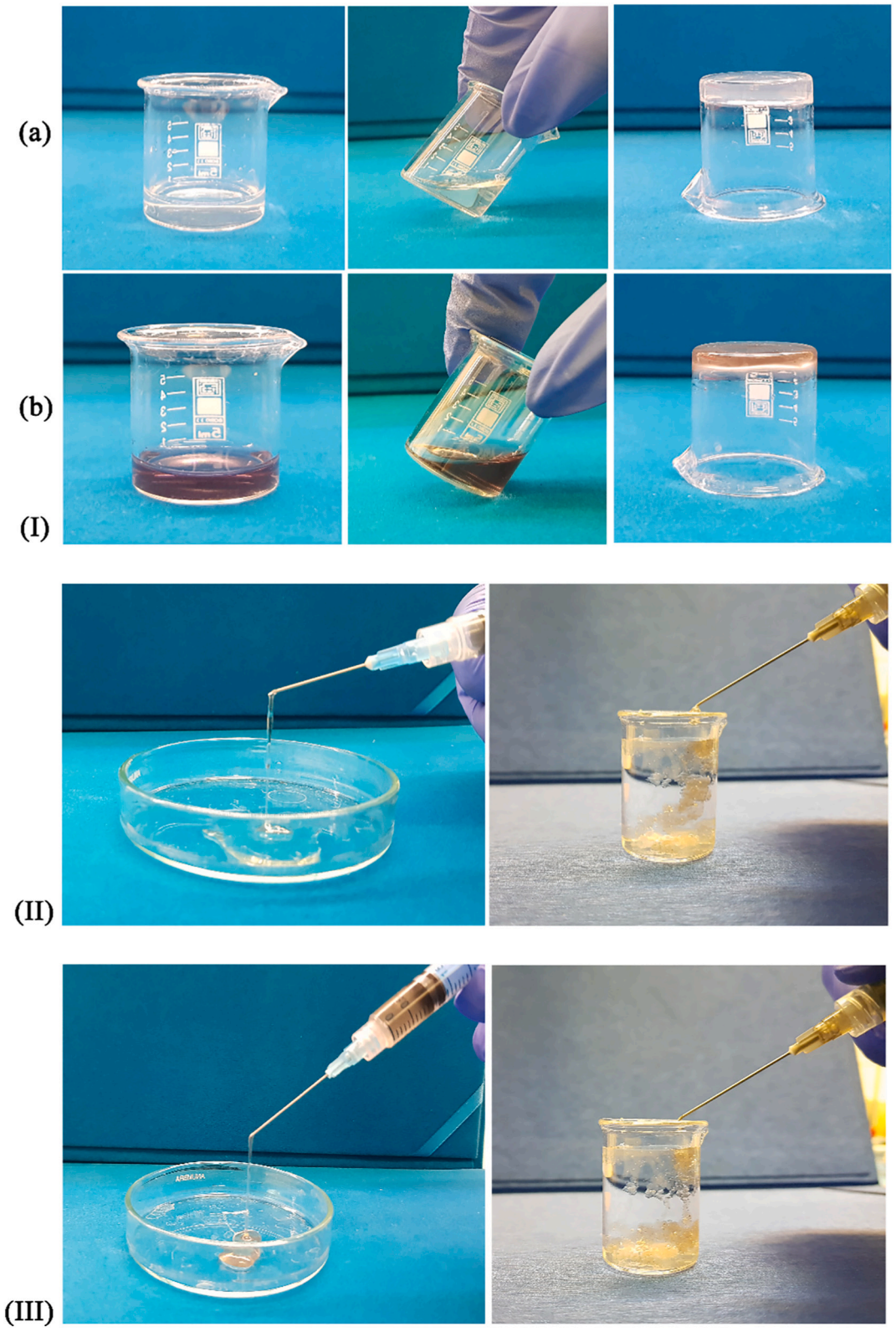

Fig. 4. (I) Phase transition and gel formation of electroactive injectable SF/PAAm hydrogels. a) before and b) after adding AP powder by using APS and continues stirring at 50 °C. (II) Injectability of the hydrogels without AP and the hydrogel injected into PBS solution. (III) Injectability of the hydrogel containing AP and the hydrogel injected into PBS solution.

through the syringe, confirming the injectability of the prepared hydrogel. Furthermore, the hydrogels were injected into a glass beaker containing PBS to verify the fact that they are injectable while preserving their shape and integrity in the solution (Fig. 4 (II) and (III)).

Recently, conductive materials are growing interest for osteogenesis induction because bone tissue is inherently conductive. Conductive materials promote bone regeneration by activating Ca^{2+}-sensitive receptors on the cell membranes that increase the intracellular level of

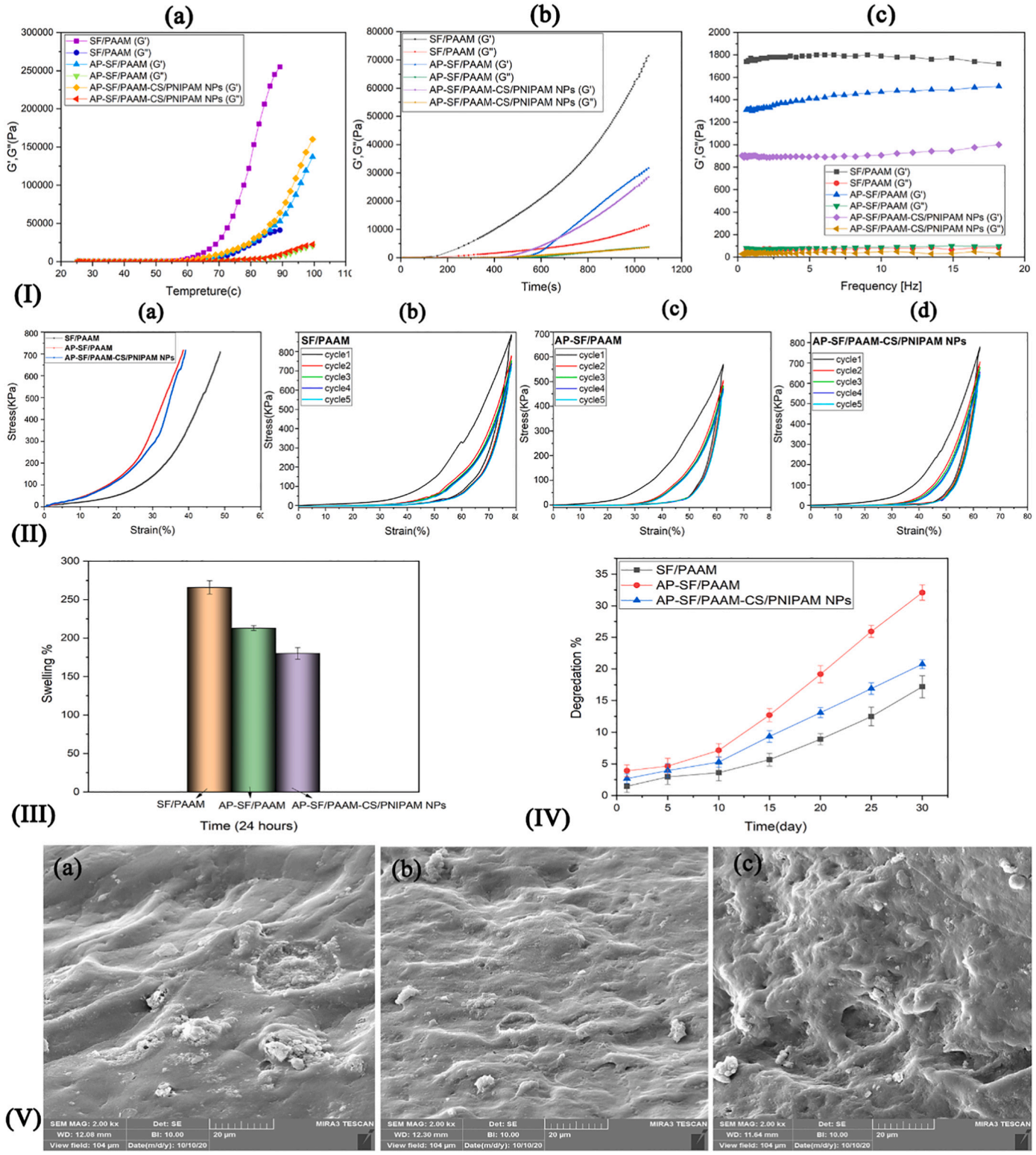

Fig. 5. (I) a) Typical temperature-dependence functions of G′ values for SF/PAAm, AP-SF/PAAm, and AP-SF/PAAm containing CS/PNIPAM NPs hydrogels at various temperatures between 25 and 110 °C. b) gelation time of SF/PAAm, AP-SF/PAAm, and AP-SF/PAAm containing CS/PNIPAM NPs hydrogels at different time points (0–1200 s). c) Frequency-dependent changes of G′ and G″ values for SF/PAAm, AP-SF/PAAm, and AP-SF/PAAm containing CS/PNIPAM NPs hydrogels at 1% strain (linear viscoelastic range) in range at a frequency of 1–10 Hz at room temperature. (II) Mechanical properties of hydrogels: a) Stress-strain curve of SF/PAAm, AP-SF/PAAm, and AP-SF/PAAm containing CS/PNIPAM NPs hydrogels by compression, b) The cycling profiles of stress-strain for the SF/PAAm, c) AP-SF/PAAm, and d) AP-SF/PAAm containing CS/PNIPAM NPs hydrogels at various strain under compression mode. (III) The swelling ratio of SF/PAAm, AP-SF/PAAm, and AP-SF/PAAm containing CS/PNIPAM NPs hydrogels at 37 °C after 24 h. (IV) The degradation of SF/PAAm, AP-SF/PAAm, and AP-SF/PAAm containing CS/PNIPAM NPs hydrogels at 37 °C after 30 days. (V) The FESEM of a) SF/PAAm, b) AP-SF/PAAm, and c) AP-SF/PAAm containing CS/PNIPAM NPs hydrogels with 2.00 KX magnification.

Ca^{2+} [47,48]. In addition, conductive materials can scavenge reactive oxygen species (ROS), which protect the tissues from injuries [49]. Among different conductive materials, polyaniline is a famous material due to its broad applications, unique structure and easy doping process, and good thermal and chemical stability [17,18]. However, its hydrophobicity and low degradation rate are two main disadvantages that limit its applications, especially in biomedical and tissue engineering fields. For this, AP with better solubility, biodegradability, and conductivity can be used as a potential alternative to polyaniline. In this work, the conductivity of SF/PAAm hydrogel at their swollen state without AP was 8.326×10^{-9} S/cm, and it reached 4.6×10^{-7} S/cm after adding AP. Significant conductivity was observed by adding AP; however, it still did not significantly increase the conductivity because low amounts of AP (0.5 mg) were used in the hydrogel. It should be noticed that before the addition of AP to the hydrogel, we conducted an MTT assay to find out the cytotoxicity of the AP in a determined concentration. The results showed that AP with concentrations above 0.5 mg had some cell cytotoxicity degrees (data reported in the MTT section). Therefore, the maximum concentration of AP with proper biocompatibility was used in the current study. However, many studies reported that high AP concentrations were needed to achieve suitable electro conductivity for bioelectrical signalling induction [45,50,51]. We also previously showed that by using 0.1 g AP, the conductivity of the hydrogel was about 10^{-4} S/cm, which was suitable for repairing hippocampus defects [21]. However, it is necessary to use optimum concentrations of AP to reach appropriate conductivity because high concentrations of aniline could decrease the conductivity due to the hindrance effect against water molecule diffusion [52].

3.5. Rheological, mechanical, swelling, degradation, and surface morphology of electroactive injectable AP-SF/PAAm hydrogels

Although the biological properties of the materials are essential for biomaterial applications, the mechanical and viscoelastic characteristics of the hydrogels are critical features to precisely assess the hydrogel characteristics. Rheology is one of the most famous experimental methods to discover the hydrogel's gelation temperature, time, and viscoelastic properties. Firstly, the AP-SF/PAAm hydrogel's rheological properties were evaluated to determine the gelation temperature. At temperatures under 65 °C, all the hydrogel solutions, including SF/PAAm, AP-SF/PAAm, and AP-SF/PAAm containing CS/PNIPAM NPs, were in the solution phase and no gelation phase was observed. At this temperature, G′ values were plateaued and then sharply increased at over 65 °C. The phase transitions were observed at about 65, 80, and 83 °C for SF/PAAm, AP-SF/PAAm, and AP-SF/PAAm containing CS/PNIPAM NPs groups, respectively (Fig. 5 (I) a). As it is clear, by introducing both AP and NPs in the hydrogels, the gelation temperature was significantly increased compared with SF/PAAm. By increasing the temperature, the hydrophobic interactions occurred between the polymer chains, and then the polymer transformed into globular and gelation phases.

Similarly, it was reported that the gelation temperature of Poloxamer 407 containing solid lipid NPs was higher (29 ± 0.7 °C) than those without NPs (26 ± 0.8 °C) due to disturbed micellar packing and entanglements of the polymeric network [53]. After blending SF with PAAm, the gelling time for SF/PAAm, AP-SF/PAAm, and AP-SF/PAAm containing CS/PNIPAM NPs were observed for about 3, 6, and 5 min, respectively (Fig. 5 (I) b). Accordingly, by adding AP and NPs to the hydrogels, the gelling time was increased nearly two-fold more than bare SF/PAAm hydrogel. Ravanbakhsh et al. reported that adding high carbon nanotube concentrations into glycol CS hydrogel could increase the gelation time due to slow and inadequate crosslinking of the hydrogel network [54]. Furthermore, an oscillatory rheology test was further carried out to assess the viscoelastic properties of the hydrogels before and after the addition of NPs. Both G′ and G″ values of all hydrogels had a nearly ascending trend by increasing the frequency. Compared with the G″ value, the value of G′ was higher over the entire frequency range, indicating the elastic and stable properties of the hydrogels (Fig. 5 (I) c). So to speak, lower G″ than G′ indicates that the elasticity properties of the hydrogels were prominent than the viscosity of the hydrogels [55]. The G′ of the hydrogels was almost linearly within the sweeping frequency interval. By insertion of AP and NPs into the hydrogels, the G′ values decreased, attributed to the weak interfacial interactions between the polymeric hydrogels with powders. Generally, the G′ parameter and the ratio of G′ to G″ have been considered to examine the mechanical properties. Typically, the hydrogels with high mechanical characteristics have high G′ with their G′/G″ balance more significant than ten or higher [56]. The stiffness of the hydrogels also correlates to the G′/G″ ratio. The hydrogels with higher stiffness are more suitable for bone regenerations. Based on the rheology analysis, it was found that all three types of the hydrogels had suitable mechanical properties; however, they were reduced by introducing powder phases.

Compression stress-strain measurements were conducted to assess the mechanical behavior of the hydrogels. As shown in Fig. 5(II), the mechanical properties were increased effectively by incorporating particles such as AP powder or CS/PNIPAM NPs into the hydrogels. For example, the Young's modulus was 36.69, 63.67, and 59.34 KPa for SF/PAAm, AP-SF/PAAm, and AP-SF/PAAm containing CS/PNIPAM NPs groups, respectively. Moreover, successive loading-unloading cycles were carried out to know the recovery and robustness of the hydrogels. After the loading-unloading test, only a slight decrease in stress-strain curves was observed for all the recovered hydrogels compared with the original ones (Fig. 5 (II) b-d), indicating the fatigue-resistant property of the hydrogels [57].

Using hydrophilic polymers for hydrogel formation is limited because they can absorb high amounts of water and make 3D structures in the swollen state that can entrap the drugs and influence their release rates by controlling the speed of diffusions throughout the hydrogel layer of the swollen matrix [58]. The swelling capacity of the hydrogels depends on the composition of the polymers, the pH of the aqueous media, the degree of crosslinking, and the porosity percentage of the hydrogels [59]. This study observed that the maximum swelling ratio was exhibited for plain SF/PAAm hydrogel (266%). Water absorption of AP-SF/PAAm and AP-SF/PAAm containing CS/PNIPAM NPs groups were about 250 and 258%, respectively, indicating that the swelling ratio did not significantly change with the addition of the powders (Fig. 5(III)). In previous studies, we and others found out that the addition of AP could reduce the swelling ratio of the hydrogels due to their hydrophobic nature [21,26]. High swelling degrees of the hydrogels were expected because both SF and PAAm have hydrophilic functional groups (NH_2 and OH groups) that are responsible for absorbing high amounts of water. It was reported that a high swelling ratio could be suitable for surgical removal after drug release from non-biodegradable hydrogels or microfluidic-based hydrogels [60,61].

Designing hydrogels with tunable degradation rates is essential to achieve proper clinical outcomes. Gradual degradation of the implanted scaffolds creates an opportunity for the injured tissues to reach suitable regeneration in a specific therapeutic window. The ratio of degradation of all the hydrogels was under ~40% of the total weight of maximally swollen hydrogels after 30 days. The degradation rate was ~15 and 32% for the hydrogels without NPs, SF/PAAm and AP-SF/PAAm groups. It was clear that with the addition of AP, the degradation of the hydrogel was increaseed significantly ($P \leq 0.05$). However, insertion of NPs showed that the degradation rate was decreased to 18% for AP-SF/PAAm containing CS/PNIPAM NPs (Fig. 5(IV)). This observation may be related to the hydrophilicity of PNIPAM, which can absorb high amount of water, resulting in hydrolytic degradation. FESEM also showed that all the hydrogels had smooth and bumpy morphology, and the addition of powders did not affect the morphology of the hydrogels (Fig. 5(V)).

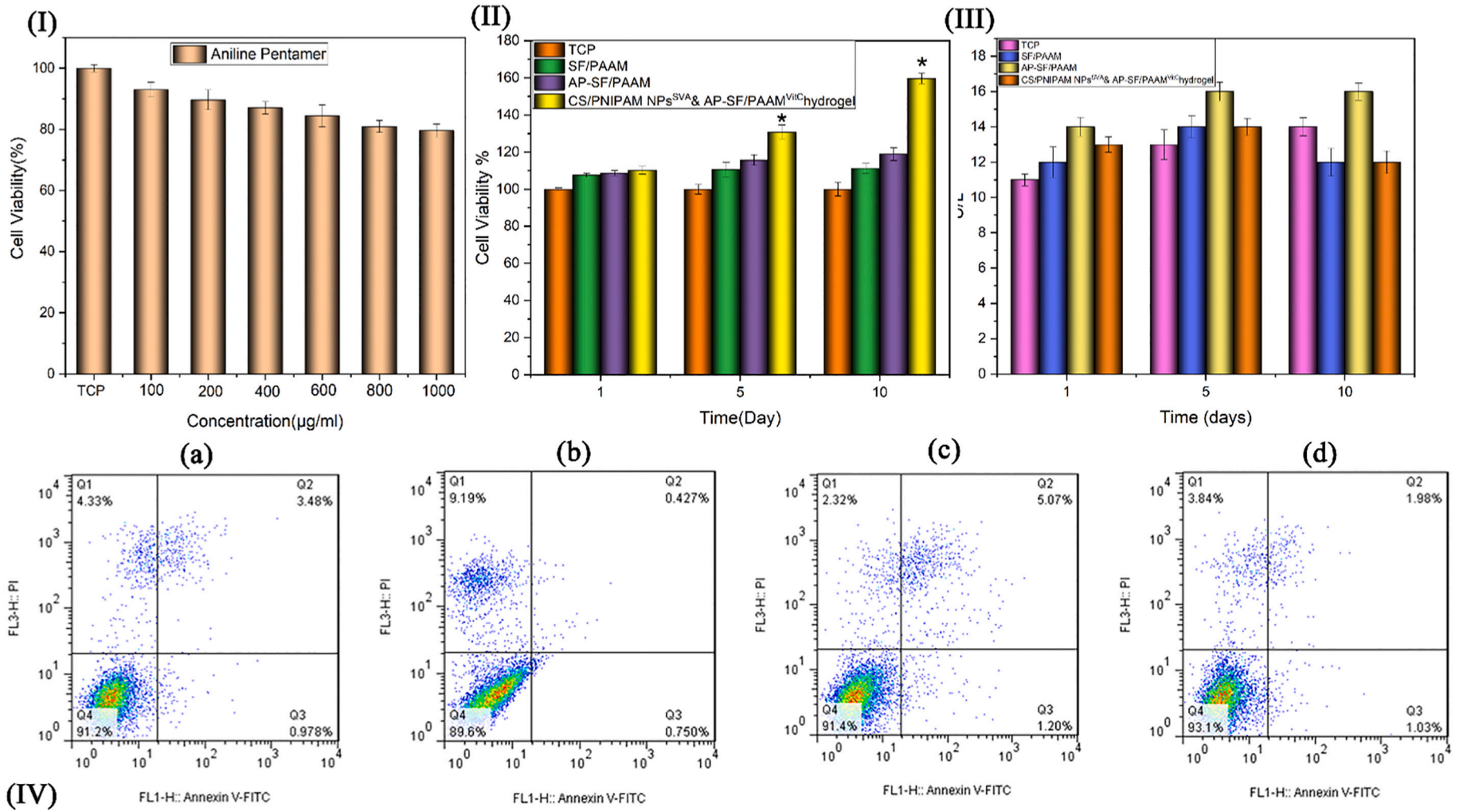

Fig. 6. *In vitro* biocompatibility studies using rabbit osteoblast cells. (I) Biocompatibility of AP powder alone at a dose of 100 to 1000 μg after 24 h. (II) biocompatibility of SF/PAAM, AP-SF/PAAM, and CS/PNIPAM NPs ^{SVA}&AP-SF/PAAM ^{VitC} hydrogels compared with TCP (as control group) at 1, 5, and 10 days. (III) LDH release from rabbit osteoblast cells after incubation in extract solutions of SF/PAAM, AP-SF/PAAM, and CS/PNIPAM NPs ^{SVA}&AP-SF/PAAM ^{VitC} hydrogels compared with TCP (as the control group) at 1, 5, and 10 days. (IV) Apoptosis analysis by using Annexin V-FITC staining that was monitored rabbit osteoblast cells after 24 h treatment in extraction solutions obtained from 10th day of a) TCP (as a control group), b) SF/PAAM, c) AP-SF/PAAM, and d) CS/PNIPAM NPs ^{SVA}&AP-SF/PAAM ^{VitC} hydrogels.

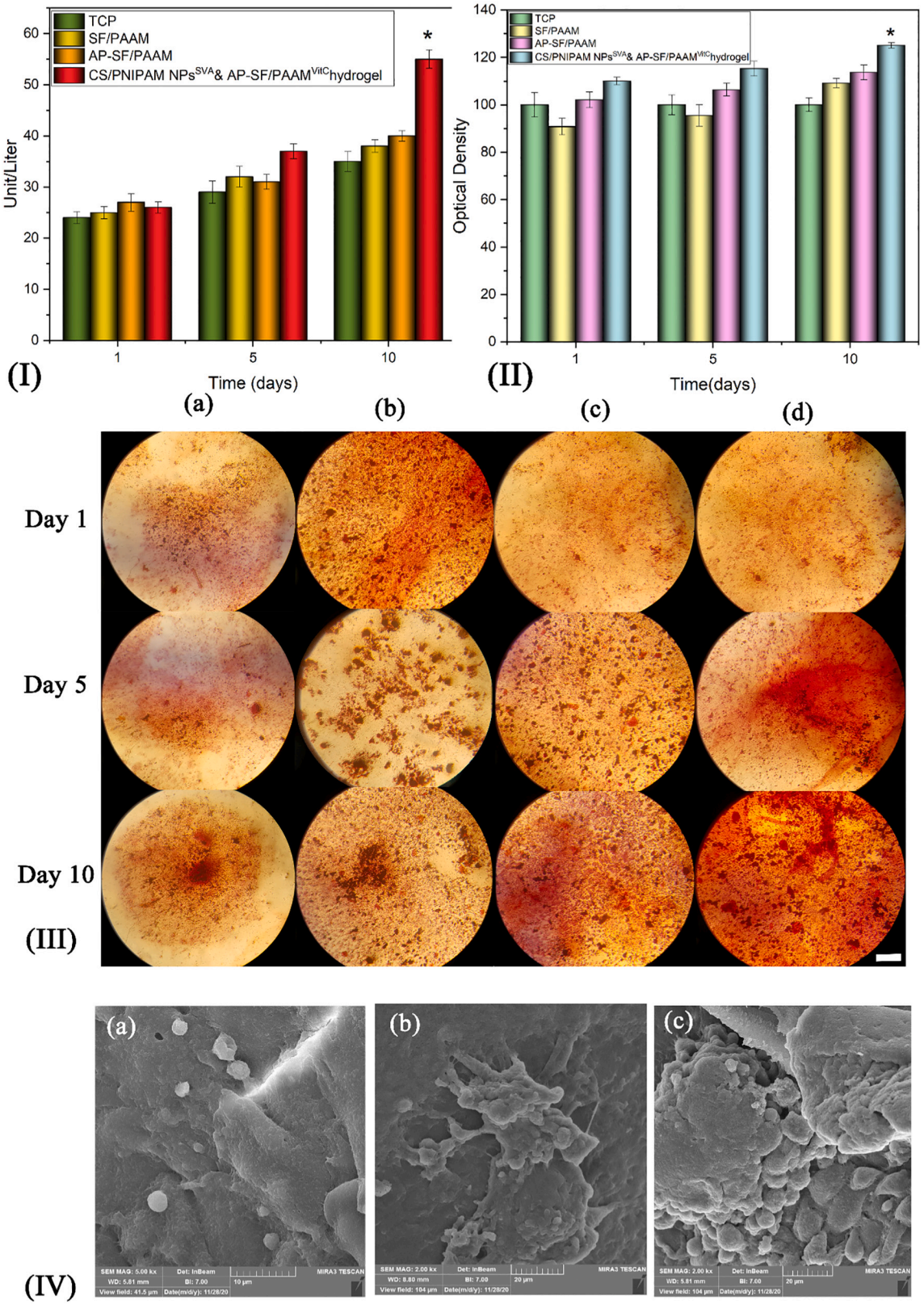

Fig. 7. (I) Expression of ALP by rabbit osteoblast cells after incubation in extract solutions of SF/PAAM, AP-SF/PAAM, and CS/PNIPAM NPs ^{SVA}&AP-SF/PAAM ^{VitC} hydrogels compared with TCP (as the control group) at 1, 5, and 10 days. (II) Quantitative and (III) Qualitative matrix mineral deposition assays by using Alizarin-Red staining of rabbit osteoblast cells after incubation in extract solutions of a) TCP (as a control group), b) SF/PAAm, c) AP-SF/PAAM, and d) CS/PNIPAM NPs ^{SVA}&AP-SF/PAAM ^{VitC} hydrogels at 1, 5, and 10 days. (IV) FESEM image of rabbit osteoblast cells after seeding on: a) SF/PAAm, b) AP-SF/PAAM, and c) CS/PNIPAM NPs ^{SVA}&AP-SF/PAAM ^{VitC} hydrogels after 24 h. *$P \leq 0.05$ (compared with TCP as control groups). Magnification for Alizarin-Red staining: 0.4 KX. Scale bar: 40 μm.

3.6. Biocompatibility of the electroactive injectable AP-SF/PAAm hydrogels

Biocompatibility of tissue engineering scaffolds is the first essential criterion for tissue engineering applications. Cells must adhere to the surface of scaffolds, function normally, migrate into scaffolds, and produce ECM [62]. Herein, the biocompatibility of AP at various concentrations was evaluated first to determine the optimum dose of AP. Many studies reported that composite scaffolds containing different concentrations of AP had acceptable biocompatibility [63,64]. However, it is hard to find studies evaluating the biocompatibility of AP powder alone. The data showed that by increasing the concentration of AP powder from 100 to 1000 μg, the biocompatibility reduced significantly in comparison to the negative control group (TCP) (Fig. 6 (I)). More cytotoxicity against rabbit osteoblast cells was observed at 800 and 1000 μg AP. It was reported that polyaniline-based powder exhibited toxicity [65] due to the presence of low-molecular-weight impurities [66]. In light of this result, we selected 500 μg AP to induce the hydrogel conductivity while having appropriate biocompatibility. Afterwards, the biocompatibility of the hydrogels was evaluated. The results showed that all the groups, including SF/PAAM, AP-SF/PAAM, and CS/PNIPAM NPs ^{SVA}&AP-SF/PAAM ^{VitC} hydrogels, had better biocompatibility compared with TCP in all time points. The best results were obtained for the group containing drugs, CS/PNIPAM NPs ^{SVA}&AP-SF/PAAM ^{VitC} hydrogels, at 5 and 10 days post-incubation due to the positive effect of SVA and VitC on the cellular proliferation (Fig. 6 (II)). It was shown that simvastatin could stimulate the human osteoblasts' proliferation through up-regulating mitochondrial function and subsequently expression of cyclin D2 and Bcl-2/Bax [67]. Further, simvastatin can suppress the TNF-α-to-Ras/Rho/MAPK pathway and stimulate the expression of ALP, BMP-2, osteopontin (OPN), and osteocalcin (OCN) during osteogenesis [68,69]. Conversely, another study showed that simvastatin decreased the cell viability and proliferation of human osteoblasts but enhanced the mineralization due to the pleiotropic effect [70]. Regarding VitC, Bose et al. observed that the addition of VitC to the β-tricalcium phosphate (β-TCP) scaffold could improve the attachment, proliferation, and viability of human osteoblast cells [71]. A similar study exhibited that using high doses of VitC had no cytotoxicity against osteoblast cell-line [72]. In addition to the MTT assay, the LDH assay was also carried out to further analyse the hydrogels. LDH has been considered a stable cytoplasmic enzyme found in various cells. Following cell damage, the cell membrane disturbs, which induces the rapid release of LDH into the cell culture supernatant. LDH results were consistent with the MTT assay. There was no significant difference between the LDH released from the hydrogels and control hydrogel groups (plain SF/PAAM), suggesting less cell membrane disruption. Although LDH synthesis increased gradually from day 1 to day 5 of culture; however, it was not significant than the control group (Fig. 6 (III)).

Apoptosis assay was further conducted to find any harmful effect of the hydrogels against rabbit osteoblast cells. This test makes it possible to detect and quantify the cellular events related to programmed cell death. Fig. 6 (IV), a-d, Q1, Q2, Q3, and Q4 indicate the cell necrosis, late apoptosis, early apoptosis, and live cells, respectively. The cells above about 90% were viable in all the groups. Late apoptosis was 1.2, 1, 0.7, and 0.9% for TCP, SF/PAAM, AP-SF/PAAM, and CS/PNIPAM NPs ^{SVA}&AP-SF/PAAM ^{VitC} hydrogels, respectively. This finding represented that the hydrogels did not stimulate the programmed cell death, confirming the results obtained from MTT and LDH assays. Generally, our results revealed no sign of cytotoxicity towards osteoblast cells by using an optimum concentration of AP in the hydrogels. Although the conductive hydrogels had better biocompatibility than plain SF/PAAM; however, it was not significant to affect the cell proliferation due to the presence of low amounts of AP in the hydrogels. Moreover, concomitant use of SVA and VitC had positive effects on the biocompatibility of the conductive hydrogels.

ALP production, matrix mineral deposition, and cells attachment on hydrogels were further carried out to assess the biological feature of the hydrogels. A similar trend to biocompatibility assays was observed for ALP production (Fig. 7 (I)) and quantities & qualities matrix mineral deposition (Fig. 7 (II) and (III)). More ALP and matrix mineral production were seen during time. Both factors were significant for CS/PNIPAM NPs ^{SVA}&AP-SF/PAAM ^{VitC} hydrogel group on the 10th day. Although ALP and matrix mineral deposition trend was ascending, no considerable production was observed on days 1 and 5. This phenomenon may be related to the low release rate of SVA and VitC. A study demonstrated that VitC enhanced ALP expression by affecting the differentiation of osteoblast cells [71]. Further, it was shown that VitC stimulated differentiation of human dental pulp mesenchymal stem cells towards osteoblast cells as confirmed by early morphological changes and nodule calcification of the differentiated cells [73].

Osteoblasts can easily adhere to the appropriate scaffolds *via* integrin receptors. Upon interaction of osteoblasts with the scaffolds, the integrin receptors transduce extracellular signals from the cell membrane, which activates the intracellular signalling pathways to control the cell growth and differentiation [74]. Rabbit osteoblast cells appropriately adhered and proliferated on the surface of all the hydrogels. Conductive hydrogels had better cell attachment than the plain SF/PAAM. Osteoblast cells also spread out and extended their filopodia on the surface of the conductive hydrogels (Fig. 7 (IV)). These results indicated that in addition to the surface topography, the conductivity of the hydrogels and using bioactive molecules had positive effects on the attachment of osteoblast cells on the substrate. The attachment of cells on the surface of the hydrogels is also affected by the mechanical characteristics of the material. The cells are able to sense and react to different mechanical properties, including surface pattern, contractility, stiffness, and dimensionality, *via* their cell membrane receptors. For example, applying tissue-engineered scaffolds with high stiffness could prevent the optimal repair of bone upon stress shielding [9]. It was also reported that MC3T3-E1 osteoblast cells were able to sense substrate stiffness and favor stiffer substrates of either hydrogels or hydrophobic surfaces with Young's moduli from ~1 kPa to ~1GPa [75–79]. Mechanotransduction refers to the cross-talk between the actin-myosin filaments with adhesion molecules like focal adhesions (FAs) and integrins [76,77]. By increasing the surface stiffness of the scaffolds, the cells better attach due to the activation of integrins and foster the maturation of FAs during cell spreading. Furthermore, the actin-myosin associations are able to conduct the mechanical signals from the biomaterial to the cell's nucleus to induce the influx of calcium ions through the cell membrane [76]. By these mechanisms, the cascade of different molecular pathways is triggered, consequently controlling the cellular behaviors in growth and differentiation.

3.7. Animal study

Micro-CT analysis has been considered a powerful method for analysis of bone ingrowth within tissue engineering scaffolds. Using this method makes it possible to study small laboratory animal models non-invasive to evaluate the structure of hard tissues. Critical-sized calvarial defects were created in aged rat models and filled with various hydrogels to find the hydrogels' regeneration ability. The first group of the animal was sacrificed at week four post-implantation. We found out that the ingrowth of new bone was very slow, which was constant in all groups based on micro-CT scans. BV% (BV/TV) was an important parameter in determining the amount of bone tissue regeneration. At this time, the BV % obtained for group 1: unfilled defect (negative control group), group 2: SF/PAAm, group 3: AP-SF/PAAm, and group 4: CS/PNIPAM NPs ^{SVA}&AP-SF/PAAM ^{VitC} hydrogel were 6.36 ± 0.5, 11.76 ± 1.1, 15.2 ± 1.4, and 19.3% ± 2.1, respectively. After eight weeks post-implantation, the negative control group exhibited minimal irregular, patchy bone formation.

In contrast, the conductive hydrogel groups, especially group 4, displayed a much more organized mineralization area towards the edge

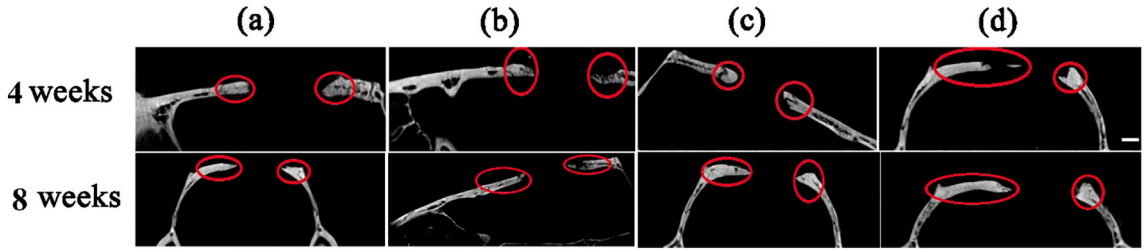

Fig. 8. *In vivo* bone regeneration based on micro-CT scans. Sagittal sections of calvarial defects filled with hydrogels at 4 and 8 weeks. a) bone sockets without hydrogel as negative control group, b) SF/PAAm, group c) AP-SF/PAAm, and d) CS/PNIPAM NPs ^{SVA}&AP-SF/PAAM ^{VitC} hydrogels. Scale bar: 10 mm. Red circle indicated new bone formation.

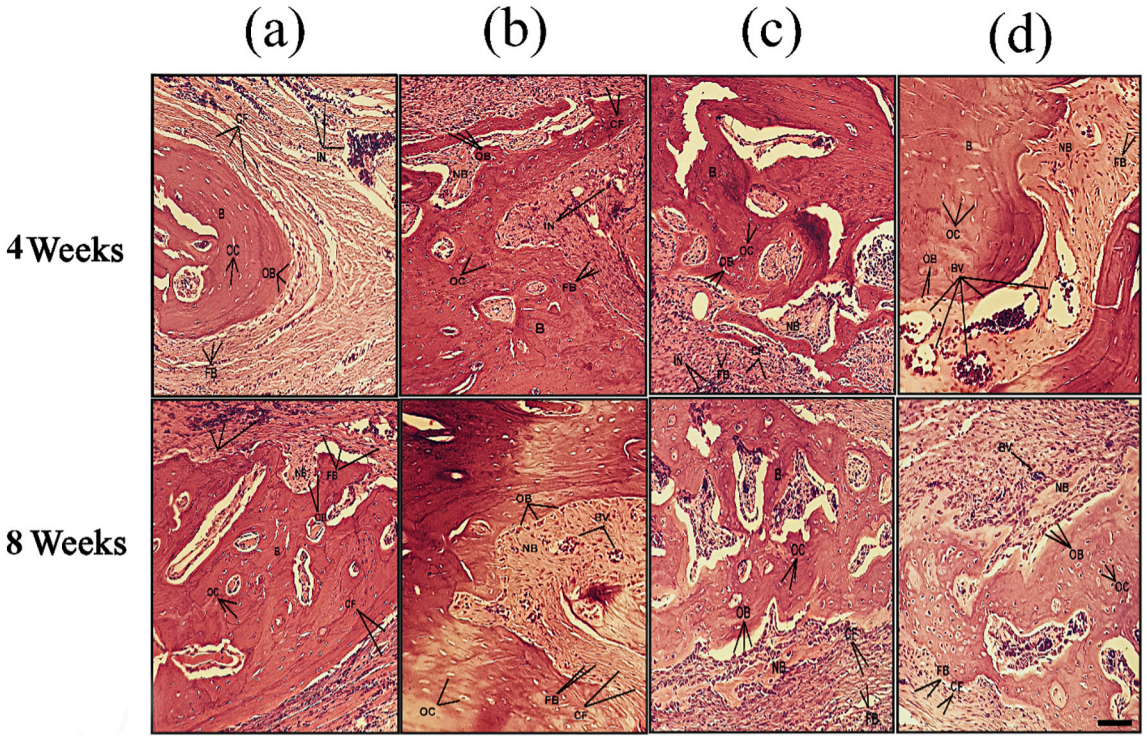

Fig. 9. Histological analysis of bone defects based on H&E staining of calvarial defects filled with hydrogels at 4 and 8 weeks. a) bone sockets without hydrogel as negative control group, b) SF/PAAm, group c) AP-SF/PAAm, and d) CS/PNIPAM NPs ^{SVA}&AP-SF/PAAM ^{VitC} hydrogels. Magnification: 0.4 KX. Scale bar: 500 μm. B: pre-existed bone, NB: new bone, BV: blood vessels, *CF*: collagen fibers, OB: osteoblasts. OC: osteocytes, FB: fibroblasts, IN: inflammatory cells.

of the defects. Based on sagittal sections of micro-CT (Fig. 8), it was observed that new bone tissue formed more towards the margin of the bone defects. The BV% parameter for groups 1 to 4 was 19.1 ± 2.5, 29.2 ± 2.2, 38.3 ± 2.9, and 61.2% ± 4.1, respectively. The statistically significant difference in bone regeneration between group 4 with group 1 may be associated with the positive effects of the incorporated drugs in the hydrogels. However, incomplete filled defects in all experimental groups may be related to using aged animal models and creating critical-sized calvarial defects.

Moreover, many studies evaluated bone regeneration at 12 weeks post-implantation; however, we analyzed bone regeneration at 4 and 8 weeks to find the regeneration potential of hydrogels at the early phase of bone healing. It should be mentioned that many studies used adult rat models and not old animals to evaluate the bone regeneration capacity of the bone scaffolds. It is hard to find studies that introduce scaffolds suitable for older people based on our knowledge. It has been established that with increasing age, the regeneration of tissue decrease. In the case of rat bone tissue, it was reported that the bone formation rate per unit of bone volume (BFR/BV) of the proximal tibial metaphysis was between 290.9% and 335.2% at 1 and 3 months of age reached 61.9% and 80.1% at 6 and 14 months of age, respectively [80]. Löffler et al. stated that insufficient bone healing in the aged rats was connected to the impaired M2 macrophage function [81]. M2 macrophages are critical immune cells that play a crucial role in tissue regeneration and angiogenesis by affecting the expression of essential factors, including IL-1, IL-10 receptor type α, and transforming growth factor-beta (TGF-β) [82,83]. Moreover, the cell differentiation and revisualization rate generally decrease with increasing the animal's age, potentially affecting bone regeneration [84].

Histology staining was carried out to analyse bone regeneration further. The different hydrogels showed some degrees of tissue ingrowth throughout the hydrogels at week 4 (Fig. 9). The control group displayed several new bone tissues compared to other groups, suggesting the critical-sized calvarial defect was difficult to self-repaired to the increase in the age of the animals. Generally, the new bone formed closely adjacent to a layer of the connective tissue within which the fibroblasts proliferate. Several osteoblast cells that synthesize osteoid were located on the surface of the new bone. Blood vessels could be observed within the defects that had a substantial role in providing nutrients and exchanging materials for surrounding cells.

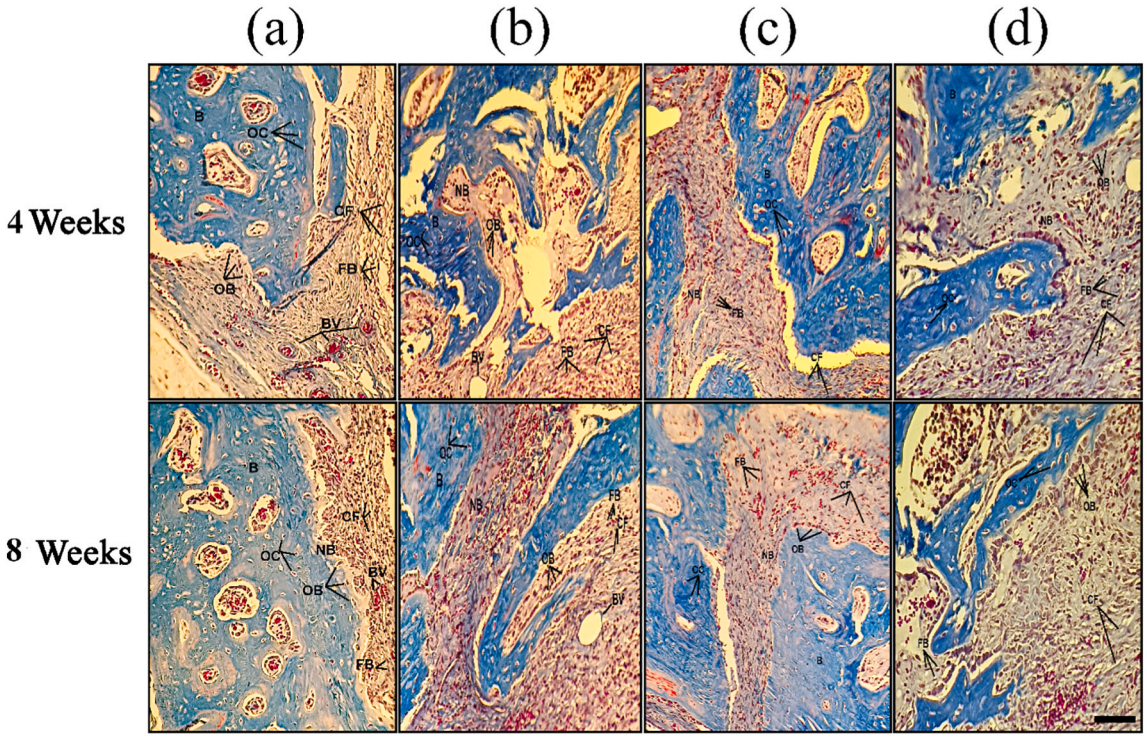

Fig. 10. Histological analysis of bone defects based on Masson's trichrome staining of calvarial defects filled with hydrogels at 4 and 8 weeks. a) bone sockets without hydrogel as negative control group, b) SF/PAAm, group c) AP-SF/PAAm, and d) CS/PNIPAM NPs ^{SVA}&AP-SF/PAAM ^{VitC} hydrogels. Magnification: 0.4 KX. Scale bar: 500 μm. B: pre-existed bone, NB: new bone, BV: blood vessels, *CF*: collagen fibers, OB: osteoblasts. OC: osteocytes, FB: fibroblasts, IN: inflammatory cells.

Further, there were remarkable amounts of inflammatory cells in the defective site, such as macrophages and lymphocytes. Compared to week 4, more bone regeneration similar to the structure of the natural bone tissue took place at week 8 (Fig. 9). According to the results obtained from Masson's trichrome staining, no remarkable fibrous tissue was observed in any of the experimental groups (Fig. 10). The defects filled with hydrogels had better collagen components and new bone formation than the control groups. Compared with other groups, this staining exhibited that abundant new collagen fibers similar to the standard architecture of mature bone with osteoblast and blood vessels were observed in the hydrogel containing drugs. Local delivery of simvastatin or VitC using proper carriers seems to be an attractive strategy to solve the problem of preserving therapeutic doses to treat non-healing bone defects and reduce undesired side effects. Simvastatin has a stimulatory role in the bone healing process by increasing the expression of BMP-2, inhibiting of osteoclasts, and stimulation of neovascularization [85]. Moreover, VitC can stimulate the proliferation of osteoblastic cells and it is responsible for the synthesis of type I procollagen mRNA and collagen fibers [86]. We suggest that simultaneous delivery of simvastatin and VitC using competent NPs and electroconductive hydrogels can improve bone regeneration in people with delayed bone repair. However, further studies are essential to optimize the hydrogel characteristics for better bone regeneration.

4. Conclusions

Thermosensitive NPs based on CS and PNIPAM was prepared for delivery of SVA. The release rate of SVA was higher at 37 °C in comparison to 23 °C, suggesting the thermosensitive properties of the NPs. Moreover, a series of injectable hydrogels based on SF and PAAm were further fabricated. AP powder was added at a non-cytotoxic concentration to endow hydrogels with conductivity. Concomitantly, the biological properties of the hydrogels were further improved by adding VitC to CS/PNIPAM NPs containing SVA. The hydrogels demonstrated suitable features, including proper injectability, stable rheological and mechanical properties, suitable swelling and degradation behaviors, excellent biocompatibility. Better cellular responses and bone regeneration were observed for the VitC and SVA hydrogels. Although the addition of AP to the hydrogels improved the cellular and animal responses; however, it was not significant compared with the plain hydrogels. These results demonstrated that electroactive injectable hydrogel containing both VitC and SVA could be considered a suitable structure for inducing bone regeneration in senescence animals.

CRediT authorship contribution statement

Negin Khaneh Zarrin: Investigation. **Fatemeh Mottaghitalab:** Visualization, Writing – original draft. **Rui L. Reis:** Writing – review & editing. **Subhas C. Kundu:** Writing – review & editing. **Mehdi Farokhi:** Supervision, Project administration, Funding acquisition.

Declaration of competing interest

The authors declare no conflict of interest.

Acknowledgement

This work has financially supported National Institute for Medical Research Development (NIMAD) Grant No. 972340. SCK has been the European Research Area Chair of the European Commission and the European Union Framework Programme for Research and Innovation Horizon 2020 (n° 668983 — FoReCaST and PTDC/BTM-ORG/28168/2017 of FCT, Portugal supported SCK.

References

[1] R. Iorio, W.J. Robb, W.L. Healy, D.J. Berry, W.J. Hozack, R.F. Kyle, D.G. Lewallen, R.T. Trousdale, W.A. Jiranek, V.P. Stamos, Orthopaedic surgeon workforce and

volume assessment for total hip and knee replacement in the United States: preparing for an epidemic, JBJS 90 (2008) 1598–1605.
[2] D. Clark, M. Nakamura, T. Miclau, R. Marcucio, Effects of aging on fracture healing, Curr. Osteoporos. Rep. 15 (2017) 601–608.
[3] M. Aflori, Smart nanomaterials for biomedical applications—a review, Nanomaterials 11 (2021) 396.
[4] Y. Kotsuchibashi, M. Ebara, T. Aoyagi, R. Narain, Recent advances in dual temperature responsive block copolymers and their potential as biomedical applications, Polymers 8 (2016) 380.
[5] T. Ueki, Stimuli-responsive polymers in ionic liquids, Polym. J. 46 (2014) 646–655.
[6] Y. Kotsuchibashi, Recent advances in multi-temperature-responsive polymeric materials, Polym. J. 52 (2020) 681–689.
[7] A. Bordat, T. Boissenot, J. Nicolas, N. Tsapis, Thermoresponsive polymer nanocarriers for biomedical applications, Adv. Drug Deliv. Rev. 138 (2019) 167–192.
[8] M.A. Mohammed, J. Syeda, K.M. Wasan, E.K. Wasan, An overview of chitosan nanoparticles and its application in non-parenteral drug delivery, Pharmaceutics 9 (2017) 53.
[9] H. Jung, M.-K. Jang, J.-W. Nah, Y.-B. Kim, Synthesis and characterization of thermosensitive nanoparticles based on PNIPAAm core and chitosan shell structure, Macromol. Res. 17 (2009) 265–270.
[10] J. Liu, Y. Cui, Y. Kuang, S. Xu, Q. Lu, J. Diao, N. Zhao, Hierarchically porous calcium–silicon nanosphere-enabled co-delivery of microRNA-210 and simvastatin for bone regeneration, J. Mater. Chem. B 9 (2021) 3573–3583.
[11] S. Zhao, S. Yu, D. Zhu, L. Dai, P. Yang, X. Xing, Stimulatory effects of simvastatin on bone regeneration of the expanded suture in rats, Am. J. Transl. Res. 12 (2020) 1767.
[12] D.H. Yang, M.S. Bae, L. Qiao, D.N. Heo, J.B. Lee, W.J. Lee, J.H. Park, D.-W. Lee, Y.-S. Hwang, I.K. Kwon, In vitro evaluation of simvastatin acid (SVA) coated beta-tricalcium phosphate (β-TCP) particle on bone tissue regeneration, Macromol. Res. 20 (2012) 754–761.
[13] M. Farokhi, F. Mottaghitalab, R.L. Reis, S. Ramakrishna, S.C. Kundu, Functionalized silk fibroin nanofibers as drug carriers: advantages and challenges, J. Control. Release 321 (2020) 324–347.
[14] H.Y. Zheng, B. Zuo, Functional silk fibroin hydrogels: preparation, properties and applications, J. Mater. Chem. B 9 (2020) 1238–1258.
[15] A.V. Torres-Figueroa, C.J. Pérez-Martínez, T.D. Castillo-Castro, E. Bolado-Martínez, M.A. Corella-Madueño, A.M. García-Alegría, T.E. Lara-Ceniceros, L. Armenta-Villegas, Composite hydrogel of poly (acrylamide) and starch as potential system for controlled release of amoxicillin and inhibition of bacterial growth, J. Chem. 2020 (2020).
[16] C. Ning, Z. Zhou, G. Tan, Y. Zhu, C. Mao, Electroactive polymers for tissue regeneration: developments and perspectives, Prog. Polym. Sci. 81 (2018) 144–162.
[17] M. Farokhi, F. Mottaghitalab, M.R. Saeb, S. Shojaei, N.K. Zarrin, S. Thomas, S. Ramakrishna, Conductive biomaterials as substrates for neural stem cells differentiation towards neuronal lineage cells, Macromol. Biosci. 21 (2021) 2000123.
[18] P. Zarrintaj, E. Zangene, S. Manouchehri, L.M. Amirabad, N. Baheiraei, M. R. Hadjighasem, M. Farokhi, M.R. Ganjali, B.W. Walker, M.R. Saeb, Conductive biomaterials as nerve conduits: recent advances and future challenges, Appl. Mater. Today 20 (2020), 100784.
[19] P. Zarrintaj, B. Bakhshandeh, M.R. Saeb, F. Sefat, I. Rezaeian, M.R. Ganjali, S. Ramakrishna, M. Mozafari, Oligoaniline-based conductive biomaterials for tissue engineering, Acta Biomater. 72 (2018) 16–34.
[20] Z. Ahmadi, N.P.S. Chauhan, P. Zarrintaj, A.B. Khiabani, M.R. Saeb, M. Mozafari, Experimental procedures for assessing electrical and thermal conductivity of polyaniline, in: Fundamentals and Emerging Applications of Polyaniline, Elsevier, 2019, pp. 227–258.
[21] M. Nourbakhsh, P. Zarrintaj, S.H. Jafari, S.M. Hosseini, S. Aliakbari, H. G. Pourbadie, N. Naderi, M.I. Zibaii, S.S. Gholizadeh, J.D. Ramsey, Fabricating an electroactive injectable hydrogel based on pluronic-chitosan/aniline-pentamer containing angiogenic factor for functional repair of the hippocampus ischemia rat model, Mater. Sci. Eng. C 117 (2020), 111328.
[22] P. Aghajanian, S. Hall, M.D. Wongworawat, S. Mohan, The roles and mechanisms of actions of vitamin C in bone: new developments, J. Bone Miner. Res. 30 (2015) 1945–1955.
[23] R.A. Shapi'i, S.H. Othman, N. Nordin, R.K. Basha, M.N. Naim, Antimicrobial properties of starch films incorporated with chitosan nanoparticles: in vitro and in vivo evaluation, Carbohydr. Polym. 230 (2020) 115602.
[24] L. Chen, Y.-H. Yu, H.-P. Mao, X.-F. Lu, W.-J. Zhang, Y. Wei, Synthesis of amino-capped aniline pentamer and UV-vis spectral study, Chem. J. Chin. Univ. 25 (2004) 1768–1770.
[25] J. Hu, L. Huang, X. Zhuang, X. Chen, Y. Wei, X. Jing, A new oxidation state of aniline pentamer observed in water-soluble electroactive oligoaniline-chitosan polymer, J. Polym. Sci., Part A: Polym. Chem. 46 (2008) 1124–1135.
[26] P. Zarrintaj, B. Bakhshandeh, I. Rezaeian, B. Heshmatian, M.R. Ganjali, A novel electroactive agarose-aniline pentamer platform as a potential candidate for neural tissue engineering, Sci. Rep. 7 (2017) 1–12.
[27] M. Farokhi, F. Mottaghitalab, J. Hadjati, R. Omidvar, M. Majidi, A. Amanzadeh, M. Azami, S.M. Tavangar, M.A. Shokrgozar, J. Ai, Structural and functional changes of silk fibroin scaffold due to hydrolytic degradation, J. Appl. Polym. Sci. 131 (2014).
[28] Y. Wang, X. Pang, J. Luo, Q. Wen, Z. Wu, Q. Ding, L. Zhao, L. Yang, B. Wang, S. Fu, Naproxen nanoparticle-loaded thermosensitive chitosan hydrogel for prevention of postoperative adhesions, ACS Biomater. Sci. Eng. 5 (2019) 1580–1588.
[29] H. Li, Q. Ji, X. Chen, Y. Sun, Q. Xu, P. Deng, F. Hu, J. Yang, Accelerated bony defect healing based on chitosan thermosensitive hydrogel scaffolds embedded with chitosan nanoparticles for the delivery of BMP2 plasmid DNA, J. Biomed. Mater. Res. A 105 (2017) 265–273.
[30] Y.-H. Cheng, Y.-C. Ko, Y.-F. Chang, S.-H. Huang, C.J.-L. Liu, Thermosensitive chitosan-gelatin-based hydrogel containing curcumin-loaded nanoparticles and latanoprost as a dual-drug delivery system for glaucoma treatment, Exp. Eye Res. 179 (2019) 179–187.
[31] M. Sareethammanuwat, S. Boonyuen, P. Arpornmaeklong, Effects of beta-tricalcium phosphate nanoparticles on the properties of a thermosensitive chitosan/collagen hydrogel and controlled release of quercetin, J. Biomed. Mater. Res. A 109 (2021) 1147–1159.
[32] N.S. Rejinold, P. Sreerekha, K. Chennazhi, S. Nair, R. Jayakumar, Biocompatible, biodegradable and thermo-sensitive chitosan-g-poly (N-isopropylacrylamide) nanocarrier for curcumin drug delivery, Int. J. Biol. Macromol. 49 (2011) 161–172.
[33] N.S. Rejinold, K. Chennazhi, S. Nair, H. Tamura, R. Jayakumar, Biodegradable and thermo-sensitive chitosan-g-poly (N-vinylcaprolactam) nanoparticles as a 5-fluorouracil carrier, Carbohydr. Polym. 83 (2011) 776–786.
[34] M. Danaei, M. Dehghankhold, S. Ataei, F. Hasanzadeh Davarani, R. Javanmard, A. Dokhani, S. Khorasani, M. Mozafari, Impact of particle size and polydispersity index on the clinical applications of lipidic nanocarrier systems, Pharmaceutics 10 (2018) 57.
[35] P. Eaton, P. Quaresma, C. Soares, C. Neves, M. De Almeida, E. Pereira, P. West, A direct comparison of experimental methods to measure dimensions of synthetic nanoparticles, Ultramicroscopy 182 (2017) 179–190.
[36] V. Bansal, P.K. Sharma, N. Sharma, O.P. Pal, R. Malviya, Applications of chitosan and chitosan derivatives in drug delivery, Adv. Biol. Res. 5 (2011) 28–37.
[37] W.K. Delan, M. Zakaria, B. Elsaadany, A.N. ElMeshad, W. Mamdouh, A.R. Fares, Formulation of simvastatin chitosan nanoparticles for controlled delivery in bone regeneration: optimization using Box-Behnken design, stability and in vivo study, Int. J. Pharm. 577 (2020), 119038.
[38] T.G. Park, Temperature modulated protein release from pH/temperature-sensitive hydrogels, Biomaterials 20 (1999) 517–521.
[39] L. Chen, M. Subirade, Alginate–whey protein granular microspheres as oral delivery vehicles for bioactive compounds, Biomaterials 27 (2006) 4646–4654.
[40] I. Karakurt, A. Aydoğdu, S. Çıkrıkcı, J. Orozco, L. Lin, Stereolithography (SLA) 3D printing of ascorbic acid loaded hydrogels: a controlled release study, Int. J. Pharm. 584 (2020), 119428.
[41] M. Moaddab, J. Nourmohammadi, A.H. Rezayan, Bioactive composite scaffolds of carboxymethyl chitosan-silk fibroin containing chitosan nanoparticles for sustained release of ascorbic acid, Eur. Polym. J. 103 (2018) 40–50.
[42] A. Sionkowska, M. Wisniewski, J. Skopinska, C.J. Kennedy, T.J. Wess, Molecular interactions in collagen and chitosan blends, Biomaterials 25 (2004) 795–801.
[43] M.-T. Nistor, A.P. Chiriac, C. Vasile, L. Verestiuc, L.E. Nita, Synthesis of hydrogels based on poly (NIPAM) inserted into collagen sponge, Colloids Surf. B Biointerfaces 87 (2011) 382–390.
[44] Y. Gong, Q.L. Liu, A.M. Zhu, Q.G. Zhang, One-pot synthesis of poly (N-isopropylacrylamide)/chitosan composite microspheres via microemulsion, Carbohydr. Polym. 90 (2012) 690–695.
[45] L. Zhang, Y. Li, L. Li, B. Guo, P.X. Ma, Non-cytotoxic conductive carboxymethyl-chitosan/aniline pentamer hydrogels, React. Funct. Polym. 82 (2014) 81–88.
[46] Y.P. Singh, J.C. Moses, N. Bhardwaj, B.B. Mandal, Injectable hydrogels: a new paradigm for osteochondral tissue engineering, J. Mater. Chem. B 6 (2018) 5499–5529.
[47] L.P. da Silva, S.C. Kundu, R.L. Reis, V.M. Correlo, Electric phenomenon: a disregarded tool in tissue engineering and regenerative medicine, Trends Biotechnol. 38 (2020) 24–49.
[48] R. Balint, N.J. Cassidy, S.H. Cartmell, Electrical stimulation: a novel tool for tissue engineering, Tissue Eng. Part B Rev. 19 (2013) 48–57.
[49] P.-A. Mouthuy, S.J. Snelling, S.G. Dakin, L. Milković, A.Č. Gašparović, A.J. Carr, N. Žarković, Biocompatibility of implantable materials: an oxidative stress viewpoint, Biomaterials 109 (2016) 55–68.
[50] Z. Bagher, Z. Atoufi, R. Alizadeh, M. Farhadi, P. Zarrintaj, L. Moroni, M. Setayeshmehr, A. Komeili, S.K. Kamrava, Conductive hydrogel based on chitosan-aniline pentamer/gelatin/agarose significantly promoted motor neuron-like cells differentiation of human olfactory ecto-mesenchymal stem cells, Mater. Sci. Eng. C 101 (2019) 243–253.
[51] Y. Liu, H. Cui, X. Zhuang, Y. Wei, X. Chen, Electrospinning of aniline pentamer-graft-gelatin/PLLA nanofibers for bone tissue engineering, Acta Biomater. 10 (2014) 5074–5080.
[52] Z. Atoufi, P. Zarrintaj, G.H. Motlagh, A. Amiri, Z. Bagher, S.K. Kamrava, A novel bio electro active alginate-aniline tetramer/agarose scaffold for tissue engineering: synthesis, characterization, drug release and cell culture study, J. Biomater. Sci. Polym. Ed. 28 (2017) 1617–1638.
[53] G. Dorraj, H.R. Moghimi, Preparation of SLN-containing thermoresponsive in-situ forming gel as a controlled nanoparticle delivery system and investigating its rheological, thermal and erosion behavior, Iran. J. Pharm. Sci. 14 (2015) 347.
[54] H. Ravanbakhsh, G. Bao, N. Latifi, L.G. Mongeau, Carbon nanotube composite hydrogels for vocal fold tissue engineering: biocompatibility, rheology, and porosity, Mater. Sci. Eng. C 103 (2019), 109861.
[55] J. Wu, K. Zheng, X. Huang, J. Liu, H. Liu, A.R. Boccaccini, Y. Wan, X. Guo, Z. Shao, Thermally triggered injectable chitosan/silk fibroin/bioactive glass nanoparticle hydrogels for in-situ bone formation in rat calvarial bone defects, Acta Biomater. 91 (2019) 60–71.
[56] A.H. Clark, Structural and mechanical properties of biopolymer gels, in: Food Polymers, Gels and Colloids, 1991, pp. 322–338.

[57] Y. Liang, X. Zhao, T. Hu, B. Chen, Z. Yin, P.X. Ma, B. Guo, Adhesive hemostatic conducting injectable composite hydrogels with sustained drug release and photothermal antibacterial activity to promote full-thickness skin regeneration during wound healing, Small 15 (2019) 1900046.
[58] F.M. Carbinatto, A.D. de Castro, R.C. Evangelista, B.S. Cury, Insights into the swelling process and drug release mechanisms from cross-linked pectin/high amylose starch matrices, AsianJ. Pharm. Sci. 9 (2014) 27–34.
[59] H. Holback, Y. Yeo, K. Park, Hydrogel swelling behavior and its biomedical applications, in: Biomedical Hydrogels, Elsevier, 2011, pp. 3–24.
[60] B. Johnson, D. Beebe, W. Crone, Effects of swelling on the mechanical properties of a pH-sensitive hydrogel for use in microfluidic devices, Mater. Sci. Eng. C 24 (2004) 575–581.
[61] R.H. Liu, Q. Yu, D.J. Beebe, Fabrication and characterization of hydrogel-based microvalves, J. Microelectromech.Syst. 11 (2002) 45–53.
[62] F.J. O'brien, Biomaterials & scaffolds for tissue engineering, Mater. Today 14 (2011) 88–95.
[63] P. Humpolíček, K.A. Radaszkiewicz, Z. Capáková, J. Pacherník, P. Bober, V. Kašpárková, P. Rejmontová, M. Lehocký, P. Ponížil, J. Stejskal, Polyaniline cryogels: biocompatibility of novel conducting macroporous material, Sci. Rep. 8 (2018) 1–12.
[64] L. Huang, J. Hu, L. Lang, X. Wang, P. Zhang, X. Jing, X. Wang, X. Chen, P.I. Lelkes, A.G. MacDiarmid, Synthesis and characterization of electroactive and biodegradable ABA block copolymer of polylactide and aniline pentamer, Biomaterials 28 (2007) 1741–1751.
[65] P. Humpolicek, V. Kasparkova, P. Saha, J. Stejskal, Biocompatibility of polyaniline, Synth. Met. 162 (2012) 722–727.
[66] V. Kašpárková, P. Humpolíček, J. Stejskal, J. Kopecká, Z. Kuceková, R. Moučka, Conductivity, impurity profile, and cytotoxicity of solvent-extracted polyaniline, Polym. Adv. Technol. 27 (2016) 156–161.
[67] S.-C. Chuang, H.-J. Liao, C.-J. Li, G.-J. Wang, J.-K. Chang, M.-L. Ho, Simvastatin enhances human osteoblast proliferation involved in mitochondrial energy generation, Eur. J. Pharmacol. 714 (2013) 74–82.
[68] M. Yamashita, F. Otsuka, T. Mukai, H. Otani, K. Inagaki, T. Miyoshi, J. Goto, M. Yamamura, H. Makino, Simvastatin antagonizes tumor necrosis factor-α inhibition of bone morphogenetic proteins-2-induced osteoblast differentiation by regulating smad signaling and Ras/Rho-mitogen-activated protein kinase pathway, J. Endocrinol. 196 (2008) 601–613.
[69] A. Montagnani, S. Gonnelli, C. Cepollaro, S. Pacini, M. Campagna, M. Franci, B. Lucani, C. Gennari, Effect of simvastatin treatment on bone mineral density and bone turnover in hypercholesterolemic postmenopausal women: a 1-year longitudinal study, Bone 32 (2003) 427–433.
[70] M.M.I. Sabandal, E. Schäfer, J. Aed, S. Jung, J. Kleinheinz, S. Sielker, Simvastatin induces adverse effects on proliferation and mineralization of human primary osteoblasts, Head Face Med. 16 (2020) 1–9.
[71] S. Bose, N. Sarkar, S. Vahabzadeh, Sustained release of vitamin C from PCL coated TCP induces proliferation and differentiation of osteoblast cells and suppresses osteosarcoma cell growth, Mater. Sci. Eng. C 105 (2019), 110096.
[72] N. Sarkar, H. Morton, S. Bose, Effects of vitamin C on osteoblast proliferation and osteosarcoma inhibition using plasma coated hydroxyapatite on titanium implants, Surf. Coat. Technol. 394 (2020), 125793.
[73] L.M. Escobar, J.D. Escobar, Z. Bendahan, J.E. Castellanos, Retinoic and ascorbic acids induce osteoblast differentiation from human dental pulp mesenchymal stem cells, J. Oral Biol. Craniofacial Res. 11 (2021) 143–148.
[74] G.B. Schneider, A. English, M. Abraham, R. Zaharias, C. Stanford, J. Keller, The effect of hydrogel charge density on cell attachment, Biomaterials 25 (2004) 3023–3028.
[75] D.E. Discher, P. Janmey, Y.-L. Wang, Tissue cells feel and respond to the stiffness of their substrate, Science 310 (2005) 1139–1143.
[76] C.S. Chen, Mechanotransduction–a field pulling together? J. Cell Sci. 121 (2008) 3285–3292.
[77] B. Geiger, J.P. Spatz, A.D. Bershadsky, Environmental sensing through focal adhesions, Nat. Rev. Mol. Cell Biol. 10 (2009) 21–33.
[78] I.A. Janson, A.J. Putnam, Extracellular matrix elasticity and topography: material-based cues that affect cell function via conserved mechanisms, J. Biomed. Mater. Res. A 103 (2015) 1246–1258.
[79] L. Cai, J. Chen, A.J. Rondinone, S. Wang, Injectable and biodegradable nanohybrid polymers with simultaneously enhanced stiffness and toughness for bone repair, Adv. Funct. Mater. 22 (2012) 3181–3190.
[80] H. Lu, L. Cui, C. Zuo, S. Lin, T. Wu, Evaluation of morphological parameters of bone formation in Sprague-Dawley rats of different ages by in vivo fluorochrome labeling, Ital. J. Zool. 82 (2015) 33–40.
[81] J. Löffler, F.A. Sass, S. Filter, A. Rose, A. Ellinghaus, G.N. Duda, A. Dienelt, Compromised bone healing in aged rats is associated with impaired M2 macrophage function, Front. Immunol. 10 (2019) 2443.
[82] N.I. Moldovan, P.J. Goldschmidt-Clermont, J. Parker-Thornburg, S.D. Shapiro, P. E. Kolattukudy, Contribution of monocytes/macrophages to compensatory neovascularization: the drilling of metalloelastase-positive tunnels in ischemic myocardium, Circ. Res. 87 (2000) 378–384.
[83] B.J. Capoccia, A.D. Gregory, D.C. Link, Recruitment of the inflammatory subset of monocytes to sites of ischemia induces angiogenesis in a monocyte chemoattractant protein-1-dependent fashion, J. Leukoc. Biol. 84 (2008) 760–768.
[84] A.L. Boskey, R. Coleman, Aging and bone, J. Dent. Res. 89 (2010) 1333–1348.
[85] M. Kheirallah, H. Almeshaly, Simvastatin, dosage and delivery system for supporting bone regeneration, an update review, J. Oral Maxillofac. Surg. Med. Pathol. 28 (2016) 205–209.
[86] F. Carinci, F. Pezzetti, A.M. Spina, A. Palmieri, G. Laino, A. De Rosa, E. Farina, F. Illiano, G. Stabellini, V. Perrotti, Effect of vitamin C on pre-osteoblast gene expression, Arch. Oral Biol. 50 (2005) 481–496.